nature nanotechnology

SUPPLEMENTARY INFORMATION

DOI: 10.1038/NNANO.2013.207

Hot-electron nanoscopy using adiabatic compression of surface plasmons

Authors: A. Giugni[1,2], B. Torre[2,3], A. Toma[1], M. Francardi[2,4], M. Malerba[1], A. Alabastri[1], R. Proietti Zaccaria[1], M. I. Stockman[5,6,7], and E. Di Fabrizio[2,4,*]

Affiliations:

[1] Nanostructures, Istituto Italiano di Tecnologia, via Morego, 30, 16163 Genova, Italy.

[2] King Abdullah University of Science and Technology, PSE and BESE Divisions, Thuwal, 23955 -6900 Kingdom of Saudi Arabia.

[3] Nanophysics, Istituto Italiano di Tecnologia, Via Morego 30, 16163 Genova, Italy.

[4] BIONEM, Bio-Nanotechnology and Engineering for Medicine, Department of experimental and clinical medicine, University of Magna Graecia Viale Europa, Germaneto, 88100 Catanzaro, Italy.

[5] Fakultät für Physik, Ludwig-Maximilians-Universität, Geschwister-Scholl-Platz 1, D-80539 München, Germany.

[6]Max-Planck-Institut für Quantenoptik, Hans-Kopfermann-Str. 1, D-85748 Garching, Germany.

[7] Department of Physics, Georgia State University, Atlanta, Georgia 30340, USA.

*Correspondence to: Enzo.DiFabrizio@KAUST.EDU.SA

© 2013 Macmillan Publishers Limited. All rights reserved.

This PDF file includes:

Materials and Methods supplementary Text about:

S1: Numerical simulation.

S2: Device fabrication and samples preparation.

S3: Optical set-up and the measurements analysis.

S4: I-V current measurement for visible 670nm and infrared 980nm excitation lines.

S5: Evaluation of the contact area.

S6: Depletion region geometry of a point contact Schottky diode.

S7: Current terms to the detected photocurrent.

S8: Schottky current in adiabatic concentrator model.

S9: Evaluation of maximum temperature increase.

S10: Photoluminescence (PL) and Absorption (ABS) characterization of GaAs sample.

S11: I-V characteristic of a n-Si/Au point contact Schottky diode and control experiments.

Figs. S1 to S26

Table S1, S2

References (*1-32*)

Materials and Methods

The device proposed in the experimental work "Hot-electron nanoscopy using adiabatic compression of surface plasmons" consists in a micrometric metallic cone with nanometric apex combined with a metalized AFM tip engineered with a grating coupler. The fabrication was realized by combining induced electron beam deposition from a Pt precursor gas at 20 keV energy for the cone growth, and focused Ga ion milling at 30 keV, for sculpturing the coupling grating. At the end the device was covered with gold using a customized sputter

© 2013 **Macmillan Publishers Limited. All rights reserved.**

coater in order to maintain the tip apex radius in the range of few tens of nanometers. The grating acts as unidirectional SPPs launcher, allowing the conversion between light and surface plasmons. Coupled SPPs flow along the tapered guiding structure of the cone, promoting the concentration of energy at its apex, where SPPs damp out as photons and hot electrons are injected directly in the semiconductor. Far field excitation, taking advantage from the propagation-induced adiabatic SPP focusing at the tip end, allows for spatially separated SPPs coupling and probe apex excitation with high signal to noise ratio field confinement and high focusing efficiency at the nanoscale.

(S1) Numerical Simulation

Simulations of the electromagnetic field distribution were performed using the commercial finite element method (FEM) based software COMSOL Multiphysics [1] for 2D grating optimization and for the final evaluation of the robustness of the photons to SPPs coupling process as function of geometrical conditions. Frequency dependent relative permittivity of gold used for the simulations was taken from Rakic's paper [2], while the refractive index of the air was set to n=1. In general, photon to SPP mode coupling undergoes the constraints of energy and momentum conservation laws. The first condition fixes the frequency, while the second, once the frequency-dependent SPP wave-vector dispersion is known [3] determines the supplementary momentum that must be provided by the grating. Accordingly to the scattering geometry sketched in Fig. S5C, we calculated the grating period *a* from

$$\frac{2\pi}{a} = \Delta K_z = K_z^{SPP} - K_z^{Ph} = \frac{\omega}{c}\sqrt{\frac{\varepsilon_d \varepsilon_m}{\varepsilon_d + \varepsilon_m}} - \frac{2\pi}{\lambda}\sin\theta_{in},$$

being ε_m and ε_d the frequency-dependent permittivity of the metal and the dielectric material, λ the free space wavelength, θ_{in} the incident angle of 36° with respect to the surface normal (fixed by geometrical constraints), z the SPP propagation direction. The calculation gives a

© 2013 **Macmillan Publishers Limited. All rights reserved.**

grating period a_1 ~ 1550 nm for the wavelength of 670 nm, a_2 ~ 2150 nm for the wavelength of 980nm, and a_3 ~ 2450 nm for the wavelength of 1060 nm. Efficient coupling requires also the optimization of the duty cycle and depth of the grating grooves [4].

We maximized the coupled power for a six grooves equally spaced 2D grating, as a function of wavelength, via numerical approach. This was assured by a convergence study. We swept routinely, one each time, all the three groove parameters: period, duty-cycle and depth for a fixed wavelength and geometry configuration, obtaining the results of Fig. S1A-C, Fig. S1E-G. All the simulations have been conducted considering a Gaussian beam defined with E_0=1 V/m on the axis. The whole device was immersed in a dielectric medium of refractive index n=1. The volume was surrounded by 5 layers of Perfect Matched Layers (PML) placed far away from the metal structures to avoid spurious effects coming from a potential interaction between the evanescent waves and the PML. In Figg. S1A-C, S1E-G we report the relative coupled power, as a function of the three groove parameters. The coupled efficiency has been defined as the ratio between two Poynting vectors, the first one integrated along a line crossing the metal surface at the far end of the grating (the white line indicated as monitor in Figg. S1D, S1H) and, the second one, integrated along a line trough the beam waist of the Gaussian incident radiation beam.

© 2013 Macmillan Publishers Limited. All rights reserved.

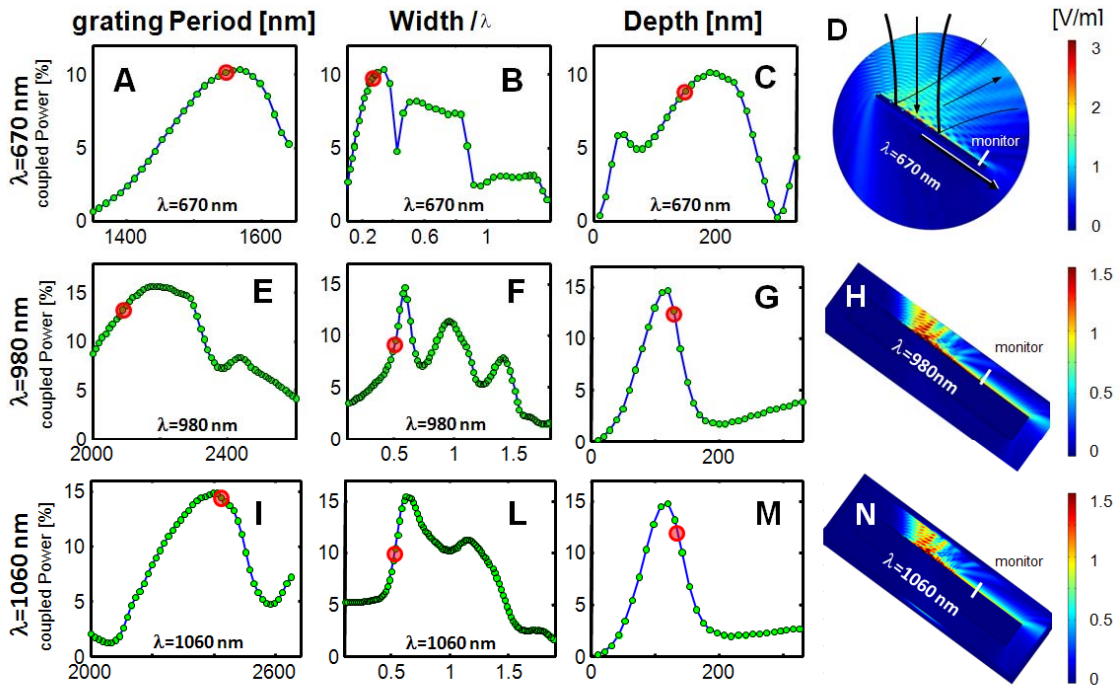

O

wavelength	grating period	width to wavelength ratio	grove depth
λ_1 = 670 nm	1550 nm	0.3	150 nm
λ_2 = 980 nm	2150 nm	0.3	140 nm
λ_3 = 1060 nm	2450 nm	0.3	140 nm

Fig. S1 (A), (B), (C), Coupled power as a function of the groove period, width to wavelength ratio, and groove depth for a wavelength of 670 nm at an incidence angle of 36.5° in respect to the grating normal, corresponding to the one adopted in the experiment. **(D)** Spatial intensity of the Poynting vector for the simulated grating of six grooves equally spaced. The corresponding parameters values are indicated as a red point in each of the upper insets (width=220 nm, depth=150 nm, groove period=1550 nm in the case of λ=670 nm). Arrows represent the main directions of the power flow. The white line indicated the position of the monitors placed along the metallic slab 5 mm apart from the grating. **(E), (F), (G),** and **(H)** report the same information as **(A), (B), (C)** and **(D)** for the λ=980 nm case. **(I), (L), (M),** and **(N)** report the same information as **(A), (B), (C)** and **(D)** for the λ=1060 nm case. Table **(O)** reports the fabricated parameters value.

The groove period is found to be the less critical parameter. Figg. S1D, S1H and S1N, show the spatial intensity of the Poynting vector, as it can be calculated according to the

© 2013 Macmillan Publishers Limited. All rights reserved.

experimental parameters. The Table in Fig. S1O, resumes the fabrication parameter adopted for the three wavelengths.

The commercial FEM CST [5] software was instead used for the 3D modelling of the device shown in Fig. S2A. Figures S2B and C are the CAD and mesh representations of the model build, starting from the optimal parameter set determined within the previous 2D simulations. A plane wave with electric field component Ex=1 V/m was sent on the front facing grating of the octagonal pyramid structure at an incidence angle of 36.5° in respect to the grating normal. Refined layers of mesh were used to terminate the nano tip apex endowed with a radius of curvature of 25 nm as depicted in the inset of Fig. S2C. This procedure guaranteed accuracy and mesh-independent results.

In order to clarify that the propagation-induced adiabatic SPP focusing at the tip apex can occur only for the TM_0 mode (radial mode) [6-7], a specific simulation was performed taking into account a sharper cone with apex radius of 10 nm (to get better evidence of the focusing phenomenon) base b = 300 nm and height h = 2.5 μm, which is quite similar to the fabricated one. Figure S2D shows the component of the electric field on a symmetry plane of the cone when either an axially aligned plane-wave (top figure) or a radial source (bottom figure) impinges on the base of the cone. Figures S2E, F, G and H show SEM images and metrology controls of the device fabricated for non-local excitation of the tip at 980 nm. In particular, Fig S2E refers to Pt cone fabrication executed after the milling of the grating and the gold coating process, while Fig. S2G show the device after the final 25 nm gold coating.

© 2013 **Macmillan Publishers Limited. All rights reserved.**

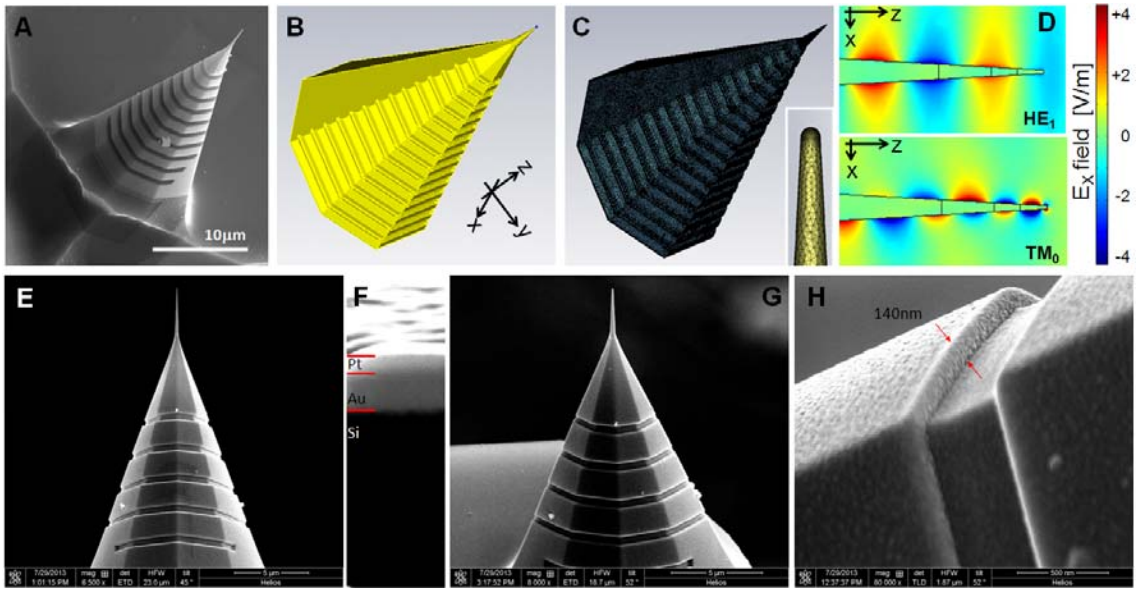

Fig. S2 (A) Scanning electron micrograph of the device fabricated for non local excitation of the tip apex at 670 nm. The grating and the cone were prepared by focused ion beam milling and induced deposition techniques, followed by gold sputtering coating procedure. (**B**) Full device structure simulated, considering optimal value of the parameters. (**C**) Mesh details of the simulated structure (refinement at the apex in the inset). (**D**) TM_0 and HE_1 x-component of the electric fields modes along the conical tip geometry, excited at 670 nm. In all cases, fields are normalized to the input amplitude, E_0=1 V/m. Only for the TM_0 case is observable the propagation-induced adiabatic SPP focusing at the tip apex. **((E) (F) (G)** and **(H)** show SEM images of the device fabricated for non local excitation of the tip at 980 nm at different realization phases and control measurements. **(E)** SEM images of the device after the grating realization, gold sputtering process and Pt cone fabrication. **(F)** Measure of the cross section of the gold coating, about 75 nm, after the deposition of a protective Pt layer. **(G)** Device after the final 25 nm gold coating. **(H)** Detail of the realized grating.

© 2013 **Macmillan Publishers Limited. All rights reserved.**

We also performed a specific numerical simulation to clarify the effect of a semiconductor surface on the plasmonic field at the tip apex. A large semiconductor spheroidal volume, defined by the dielectric constant ε_r=12.9, has been placed close to or directly in contact with the gold tip. Figures S3A and B show the electric field enhancement near the apex in a symmetric plane for the excitation at 670 nm in the two conditions. Higher field enhancement at the Au tip was observed when the contact is established [8], due to the high value of the refractive index of the semiconductor (n ~ 4.4).

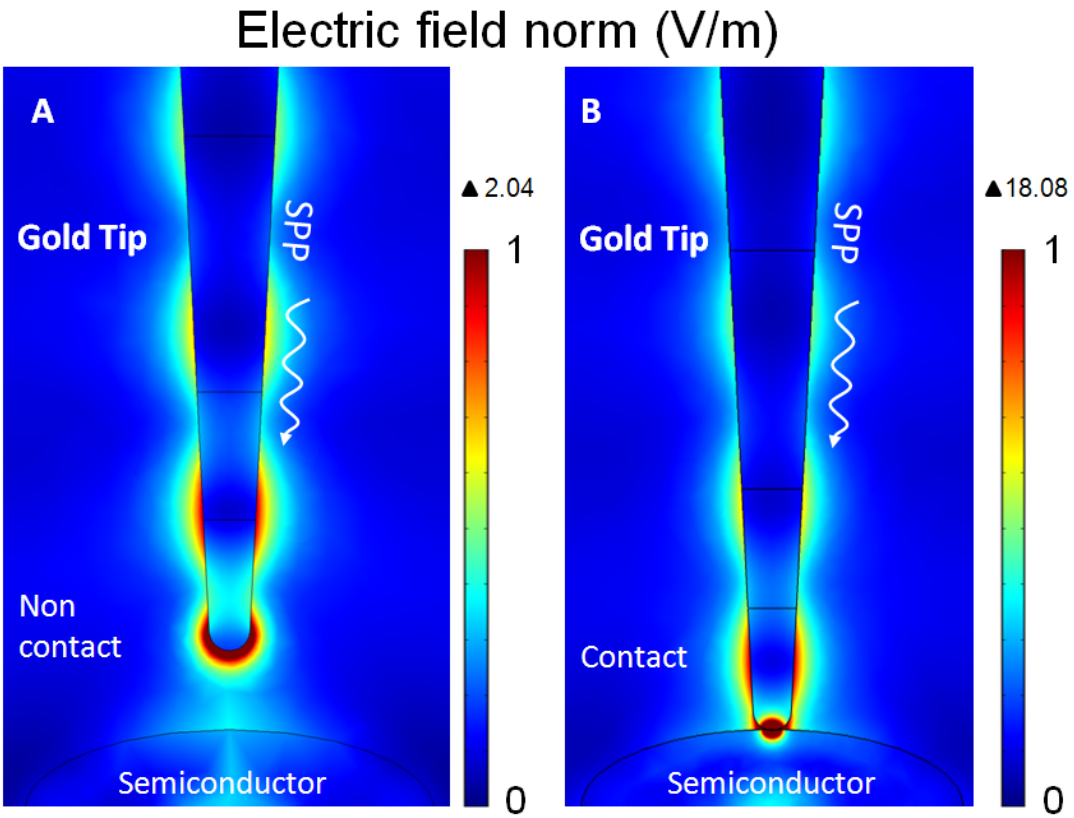

Fig. S3 Electric field norm of a TM_0 mode along the conical tip geometry (R_{tip} = 25 nm), excited at 670 nm. (**A**) The tip is in non contact with respect to the semiconductor sample. (**B**) When the tip is posed in contact with the semiconductor, a further enhancement of the induced adiabatic SPP focusing at the tip apex can be deserved. In all cases, fields are normalized to the input amplitude, E_0=1 V/m.

© 2013 Macmillan Publishers Limited. All rights reserved.

(S2) Device fabrication and sample preparation

The coupling device used to harvest and to convert the incident light into propagating SPPs was realized by means of focused ion beam (FIB) technique, by milling sub-wavelength grooves on the front face part of a pyramidal AFM tip (μ-masch csc38, n-type silicon tip, height ~ 20 μm, full tip cone angle ~ 40°) and successively sputtered with a gold layer. The separation distances and widths of the grooves were milled with a precision of ±5 nm, while the groove depths, being harder to control, were realized with a (reproducibility) precision of ±15 nm, as can be estimated from the scanning electron microscope (SEM) images reported in Fig. S4. The sharp micrometric cone (height: 2500 nm, base radius: 300 nm) was realized in a second moment using electron-beam-induced deposition, as a Pt-C cone structure with an apex radius < 10 nm. Finally, the whole structure was gold coated by means of controlled Ar^+ sputtering deposition technique to reach the final thickness of 25 nm in proximity of the tip apex. This process provides a smooth coupling between tip and cone geometry.

By exploiting the numerical results already discussed in Fig. S1 we estimated the impact of fabrication uncertainties on the experimental value of the coupling efficiency. For fixed groove spacing, equal to the nominal value, we found that a 10% overall error on all the groove widths or depths (that is worst than our experimental accuracy) can degrade the coupling efficiency of ~ 3%. Thus, we can realistically expect an experimental coupling value still of the order of the computed value, about 10%.

© 2013 Macmillan Publishers Limited. All rights reserved.

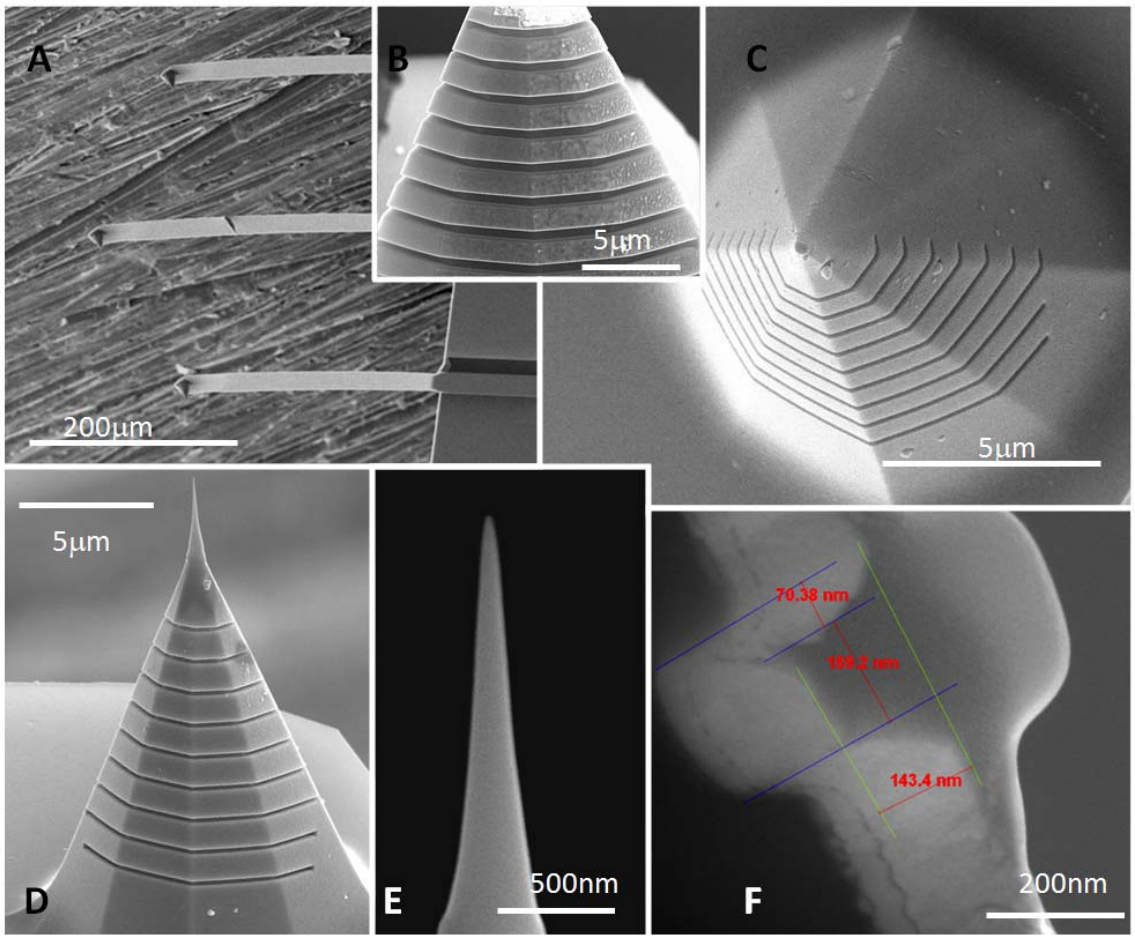

Fig. S4 Scanning electron micrographs of the device. (**A**)(**B**)(**C**)(**D**) and (**E**) SEM images illustrating the fabrication steps of the grating (used for non local excitation of the tip apex at the wavelength 670 nm) and the sharp cone, both were prepared by focused ion beam milling and induced deposition techniques, preceded and followed by gold sputtering. (**F**) Zoomed-in image of a cross section of the grating.

© 2013 **Macmillan Publishers Limited. All rights reserved.**

Samples preparation

N-type GaAs wafer (Si-doped, (100)-orientation, mobility μ = 3590-3850 $cm^2/V/s$, ρ = 0.02 Ohm·cm) was purchased from GEO Semiconductor (UK) LTD. Specimens, of approximate area 0.25 cm^2, were cleaved from the same wafer and a back (ohmic) contact was realized by using silver bonding-paste on the metallic AFM holder. GaAs wafer as-received had a gallium-rich native oxide which was not affected by solvent degreasing treatments with a bath of methanol and acetone. Thus the specimens were wet etched for 3 minutes in a solution of HCl 37% in water, in order to remove the native oxide layer, and subsequently rinsed in deionised water.

To demonstrate that the proposed scanning probe nanoscopy, based on hot electrons transfer, has chemical species sensibility, resulting in different electron transfer efficiency, we imaged the photocurrent of specific custom realized locally patterned samples. Either ion implanted conductive samples or locally oxidized surfaces, at 670 nm and 980 nm were investigated.

Direct scanning probe writing, specifically lithography by high field discharge technique on a freshly cleaned n-type GaAs substrate, was used to write down local oxidized pattern of nanometric scale (width down to 40 nm, height profile down to 0.5 nm). The writing processes have been performed in contact mode maintaining a set-point force below 10 nN. As illustrated in Figure S5C, applying a positive sample bias, GaAs local oxidation occurs, due to the formation of a localized water meniscus below the AFM tip arising from environmental humidity, (well known phenomenon for relative humidity of air exceeding 40%). This writing procedure allows features with width resolution of about 40÷60 nm (tip radius dependent) and well controlled single pass height on the nanometric scale (0.5÷4 nm, in the -2÷-14 V tip voltage range). During the procedure the tip scan, immersed in liquid meniscus, the surface at constant speed (1÷4 μm/s) according to a pre-designed pattern.. It is

© 2013 **Macmillan Publishers Limited. All rights reserved.**

possible, by easily tuning the applied bias and scan speed to control the oxidation rate, i.e. height and width of the line. The technique allows also a multi-pass writing process, until a cut off height usually occurs for semiconductors oxides at final layer thickness of about 8-10nm, even if exceptional thicknesses exceeding hundred nanometers has been recently demonstrated [9]. The oxide layers deposited with a positive biased sample were subsequently measured with the SPPs Nanoscopy setup to obtain simultaneously morphology and hot electron map current.

Figure S6 shows, as example, topography and current measurements on a multi pass local oxidized sample. There, higher squares (bright) in the topography correspond to the 1x μm^2 oxide patterned decorations, resulting in an average height of 8 ± 1.5 nm (see profile in Fig. S6B), and an increased RMS roughness in the oxide region (about 1 nm), revealing the intrinsic parallel lines texture of the deposition technique (black raster sketch in Fig. S6B) as compared with the atomically flat GaAs region (0.3nm RMS). In Fig. S6C both topography and current maps are reported, overlaid in a 3D rendering revealing the final perfect overlapping and striking resolution of the proposed imaging technique. This specific sample has been prepared using an Asylum Research MFP-3D, with gold coated SiN tips (Olympus RC800PB) in contact mode. Compositional variation has been confirmed in-situ by means of scanning Kelvin probe microscopy (Olympus OMCL AC240TM).

The highest spatial resolution pattern of Fig. 5a, and Fig. S5A were obtained writing the samples at constant speed (4 μm/s) in humid air, applying positive sample bias of few volts, with the our plasmonic device, characterized by an extremely high aspect ratio and tip radius <25 nm (see also caption of Fig. S5 for further details).

Furthermore low topography profile structured samples were prepared by means of FIB gallium-ions implanteation, resulting in an approximatively flat, locally modified conduction patterned GaAs sample. The sample patterns consist of single lines arranged in

© 2013 Macmillan Publishers Limited. All rights reserved.

grid fashion,fabricated by means of FIB technique at different ions doses. At low doses, surface amorphyzation and ion implantation occurs, resulting in amorphous doped features protruding from the surface, as imaged by SEM (Figg. S7A-B). Increasing the dose, Ion erosion prevails and the milling process starts, as producing deep structures as the square markers in Figg. S7A,B. Therefore by properly tuning the dose, low profile structures can be fabricated with a modified conductance grating. Fig. 5E, F, G, and Fig. S7 show topography and plasmonic photocurrent maps generated at 980 nm laser excitation. In this way chemical sensitivity leading to both current depletion (oxide) and increase (ion implantation) can be verified with nanometric resolution in our setup All the samples show an increased conductivity due to 30 keV implanted Ga ions, while the topography reflects, the progressive amorphization of the GaAs crystal structure (higher inter atomic distance, hence higher volume) or the ion milling effect that generates local dips in the profile. This effect is readily observable in Figg. S7 C and D, where we present topography and current maps of ion implanted GaAs at the higher dose evaluated. In the topography map it is possible to recognize a differential ion implantation process combined with surface ion milling, as thin lines protruding from the surface. The current map show an increase conductance at the features border, mainly located at the GaAs side, while in the topmost part of the feature, current is systematically reduced, as better shown by the line profile in Fig. S7E. This is interpreted as a cumulative effect of the two competitive processes, i.e. doping and amorphization on local conductance, proving the high spatial resolution on compositional and structural chemical change, which is a key feature of this technique. The overall result is a spatial resolution of the current map in the range of 100 nm.

All these experiment further support that imaging by hot electrons can efficiently work with both oxide and conductive nano-patterned structures, allowing to further resolve compositional and structural changes emerging out from topography.

© 2013 **Macmillan Publishers Limited. All rights reserved.**

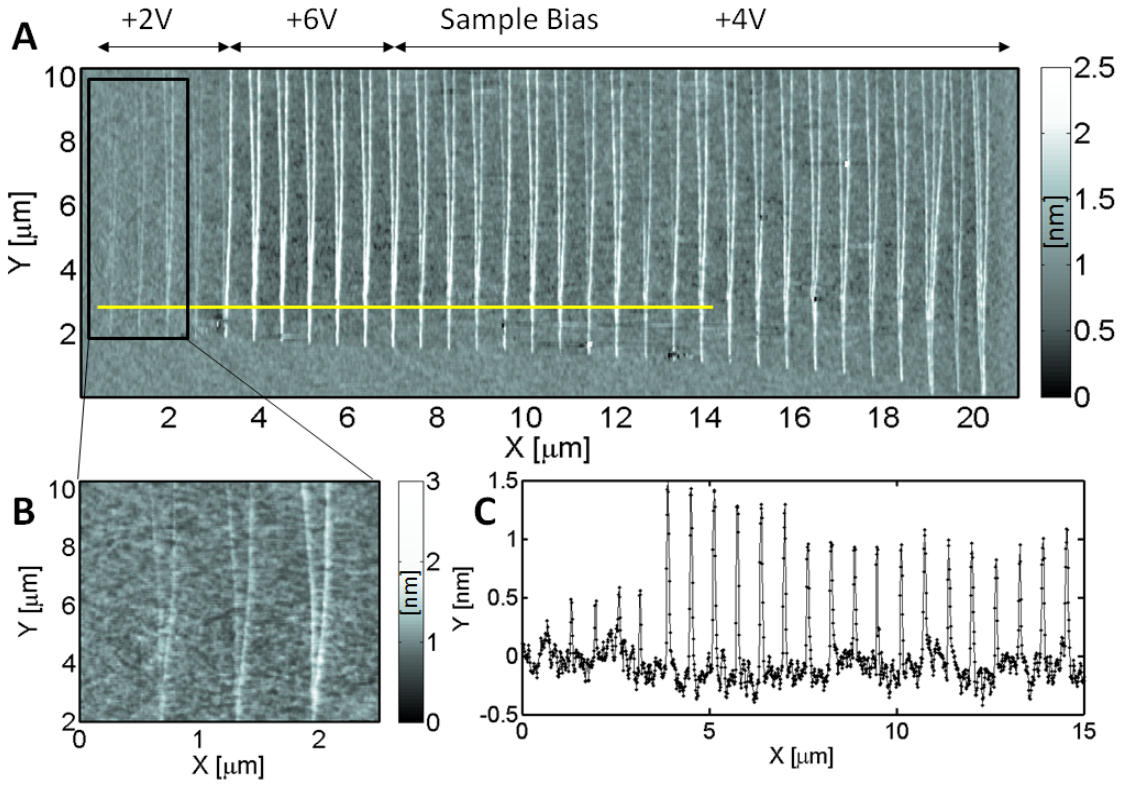

Figure S5 – AFM topography and height profiles of a continuous pattern written with different sample bias (+2 V +4 V and +6 V) at 4 μm/s writing speed, in contact mode (set point 10 nN). (Pattern and profile shown are not deconvolved for the tip profile). The pattern was written and subsequently measured scanning in contact mode the AFM, using the same conical tip used for photocurrent measurement. **(A)** AFM topography of the oxidized zig-zag profile realized on the surface of n-type GaAs sample. The chosen pattern allows easily the recognition of the limiting resolution of the adopted fabrication technique, approaching the vertices in the pattern we measured a FWHM <40 nm. The continuous long lasting line writing profile demonstrate the stability, reproducibility and control of the scanning probe lithography technique used in writing oxidized pattern of nanometric scale (height profile down to 0.5nm), as well as the stability of the fabricated tip. . The black rectangle indicates the zoomed area reported in **(B)**. It shows a detail of the pattern, relative to the thinner lines obtained in our working condition. The yellow line indicates where the height profile shown in **(C)** is measured

© 2013 **Macmillan Publishers Limited. All rights reserved.**

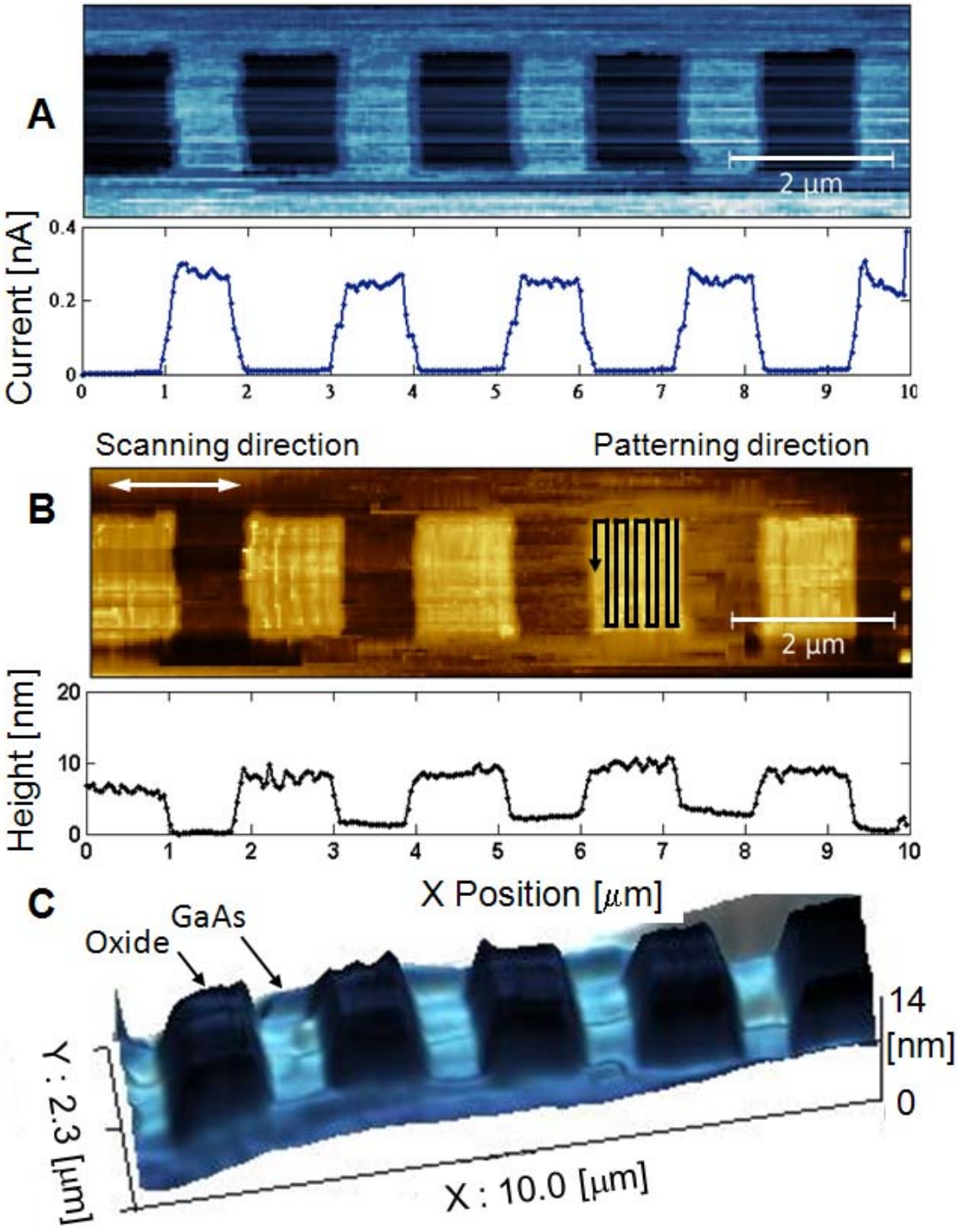

Figure S6 Photocurrent and topographic maps of oxide square pattern deposited on GaAs. **(A)**, Averaged lines profiles (over 16 lines) clearly shows the different hot electron transfer efficiency in the GaAs substrate and the oxide squared region on GaAs. **(B),** Topographic map. **(C)**, Hot electron current imaging overlaid on 3D topography to simultaneously show the achieved current and topographic resolution. The wavelength was λ_1=670 nm.

© 2013 **Macmillan Publishers Limited. All rights reserved.**

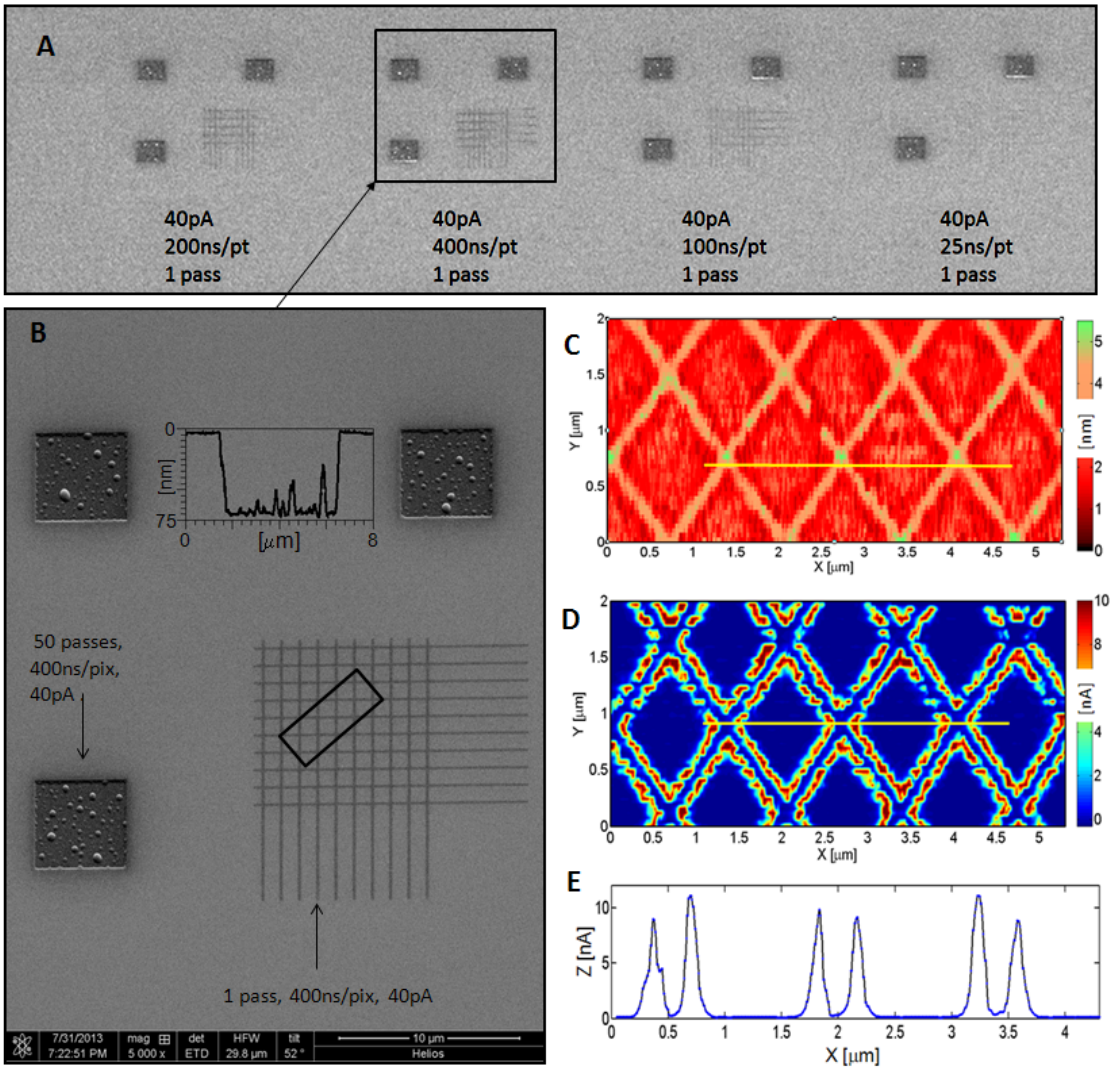

Figure S7 SEM images of gallium-ion implanted GaAs sample, topography and plasmonic photocurrent maps generated at 980nm laser excitation. **(A)** SEM image of the sample patterns fabricated as single lines arranged in grid fashion with the focus ion beam technique at different ions doses. Single pass, low current, extremely short pixel time modality was required to avoid engraving the semi conductive sample. 5x5 µm squares were realized and used as markers for optical alignment. **(B)** Zoomed SEM image detail of the highest doses pattern. The black rectangle indicates the area relative to the topography and plasmonic photocurrent maps of **(C)**. **(D)** and **(E)** show the single line photocurrent intensity indicated with a yellow line on the images.

© 2013 **Macmillan Publishers Limited. All rights reserved.**

(S3) Optical set-up, electronic scheme and measurements analysis

To measure the local photoelectric effect we have developed an *ad hoc* setup based on an Atomic Force Microscope (AFM - Bruker Multimode V), which employs an optical system adequate to properly promote the adiabatic SPP compression, and a fast high-gain current amplifying circuit, used to record the current within the range 10pA-10μA. The present set up it is briefly described in the caption of Fig. S8. Current amplification system employed either a FEMTO LCA-M-50k-100M-x transimpedance amplifier (TIA current to voltage conversion gain of 10^8 and 50 kHz (-3db) bandwidth having a very low integrated current noise over the whole bandwidth i_n=9.2 pA), or by home made two stages inverting TIA based on AD8626 OpAmp with an overall gain about 10^9 ($out_1=10^6$ $out_2=10^9$). This approach allowed two different sensitivities ~1 V/nA and ~1 V/μA, respectively with sufficient bandwidth exceeding 50 kHz. The sample was externally biased using an Agilent 81160A Pulse Function Arbitrary Noise Generator in the ±10 V range.

Immediately after transimpedance conversion, current signal was pre filtered by Stanford RESEARCH filtering unit (SIM918), applying a 24 dB/oct Bessel low pass filter at 49.7 KHz. We used it to further filter high frequency noise without introducing significant phase distortions and signal bandwidth reduction for further Lock in amplification. A fast 2 Gsample/s oscilloscope was used to routinely monitor the signals. Up to 6 signals ($I_{HighGain}$, $I_{LowGain}$, V_{Bias}, trigger signal, laser pulse profile and z-AFM position) were recorded using a National Instruments USB-6366 16 bit ±10V parallel acquisition Board, typically at 100 KHz sampling rate. All the measurements were performed in Tip-Sample contact (AFM contact mode). The photo excitation was performed by single mode lasers, vertically polarized (~along tip principal axis), at λ=670 nm (1.85 eV, single mode Omicron Redphoton® CWA Series SM) at 980 nm (1.26 eV, Choerent, FC multimode fibre coupled

© 2013 **Macmillan Publishers Limited. All rights reserved.**

laser) or λ=1060 nm (1.17eV, single mode IPG Photonic mod. YLR-5-LP). To take control of unwanted drift effects (slow drifts and acoustic excitations) typically affecting AFM measurements during the time measurement we modulated the laser amplitude with a square wave at frequency of 257 Hz, 317 Hz or 570 Hz with a duty-cycle 50%.

For the current to voltage measurements discussed in the main text, the two characteristics with and without illumination were retrieved via a post processing code written in Matlab software. It allowed the full analysis of the temporal waveform signals. For the electric map (discussed in the main text), the photo induced current was obtained via a real time demodulation of the signal with a lock-in amplifier (LIA). In particular, the reference signal was acquired from IR led-photodiode (PD) pair and used to filter out the AC part of the measured current, synchronous with the laser pulses, to finally obtain the laser induced contribution to the measured current. The current signal at the exit of the first amplifier was AC coupled with the external LIA (Stanford Research SR830) to filter out all possible contributions not synchronous with laser modulation, leaving just the laser induced component. Further, lock in phase was optimized to filter out all synchronous spourious contributions arising from capacitive couplings. Output signal was then time averaged with an integration time of 20 ms and acquired as image by AFM electronics, while the tip was scanned over the sample, resulting in a hot electron image acquired in parallel to sample topography. In this way current contribution coming from different parts of the sample were easily discriminated, as shown in Fig. 5. The mapped value was an average over the last ~8 pixels, corresponding to a spatial average of ~80 nm (10x10 μm 1024x1024 steps ~4 μm/sec ~410 pts/sec). In this regime the signal is averaged over a region wider than the contact dimension (in the range of 10 nm) and the nanometre-size depletion region of the Schottky barrier (evaluated of the order of 60nm), providing a quite acceptable smoothing effect observed in Fig. 5. A Mitutoyo 20x objective (BD Plan Apo SL20X 85% transmittance at

© 2013 Macmillan Publishers Limited. All rights reserved.

670 nm, 35% at 1060 nm) supply the laser excitation to the grating, while a confocal non polarizing beam splitter (BS) allows the collection of the scattered light to a CCD detector.

Note: current detection and filtering setup was carefully tuned and optimized to minimize spurious (capacitive) signals arising from cross talk with the illumination system. In order to reduce illumination induced capacitive signal, we performed preliminary experiments with tip retracted by some micrometers from the surface as well as with insulating samples. In this condition we found, as main source of noise, some synchronous high frequency peaks coming from power supply and a visible contribution, 90° shifted with respect to laser illumination and hot electron current signal, due to capacitive coupling between laser modulation electronics and the AFM tip. Both contributions have been minimized by means of a very careful shielding of such sources of noise and current pre-amplification system, and further reduced by means of the low pass Bessel filter, in first case, and by lock in phase optimization for the capacitive coupling. This effort resulted in a null signal with tip retracted from the surface and final Signal to Noise ratio >> 1 at moderate laser illumination power (not harmful power for the tip). The synchronous spurious contribution was negligible in the time domain acquired signal (as shown in Fig. S9), and in the further optimized integrated signal (LIA synchronous detection) acquired in parallel with topography, for the hot electron detection.

© 2013 **Macmillan Publishers Limited. All rights reserved.**

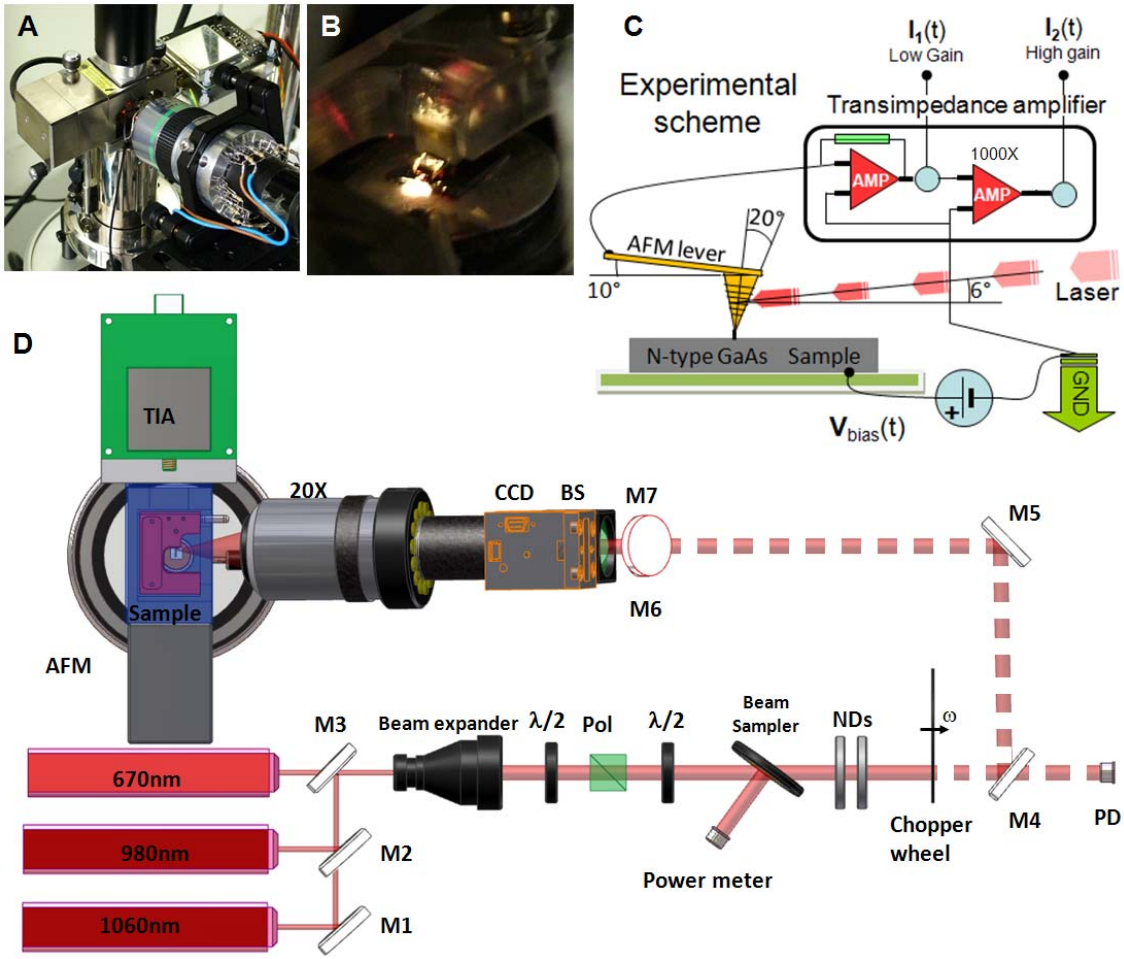

Fig. S8 Photoelectric Atomic Force Microscope. (**A**) Microscope head setup. (**B**) Close-up image of the customized AFM chip holder for current measurements. (**C**) Experimental scattering geometry and basic current circuitry scheme. Photo-generated currents are read using a TIA amplifier and eventually demodulated with a LIA, then fed into the auxiliary input of the AFM driver. (**D**) Schematics of the optical setup: three laser sources at 760 nm 980 nm and 1060 nm share a common optical path to the sample. M1 M4 M5 M6 silver mirrors, M2 flip mirror, M3 beam splitter (80:20 R:T). Laser intensity and polarization state were controlled by means of zero order wave plates (λ/2) and a broadband polarizing beam-splitter cube (Pol) and monitored by a calibrated power meter on a 8% beam sampler plate. Incoming laser was further attenuated with neutral density filters (NDs) and modulated by a mechanical chopper.

Figure S9 shows a short temporal interval, in correspondence of zero applied bias, of the waveforms measured with an adiabatic tip designed for visible radiation. Laser trigger-

© 2013 Macmillan Publishers Limited. All rights reserved.

timestamps allow the recognition of each optical cycle and the identification of data intervals not affected by transient phenomena. Data averaging is then performed to calculate the net current difference for each optical cycle and to determine the current to voltage characteristic reported in Fig. 4 Fig. S10 and Fig. S11.

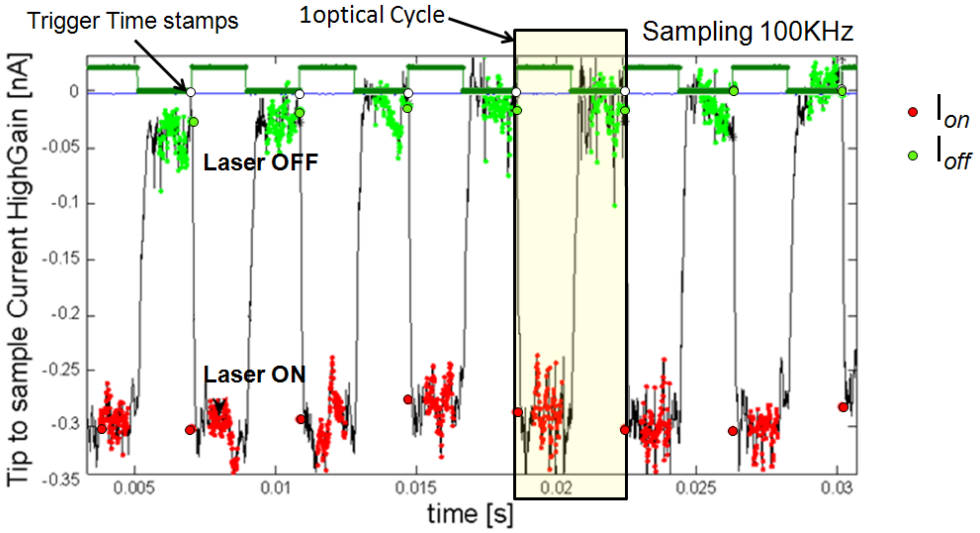

FIG. S9 Data analysis. The picture shows the temporal waveform signals of current (black), laser trigger (green) and voltage bias (blu), recorded at sampling rate of 100 kHz and 0 V bias for the 670 nm excitation. For each optical cycle, identified via software from the laser driver signal, data subsets unaffected by transient processes were identified (green and red points). Each single interval was then averaged to obtain a couple of numbers, one for each cycle, identifying the actual values of the current (big green and red points) under illumination and in dark condition at the corresponding bias.

(S4) I-V current measurement for visible 670nm and infrared 980nm excitation lines

Figure S10 reports the representative *I-V* characteristics of our plasmonic structure when photoexcited at λ=670 nm by the incoming laser (laser power impinging on the grating ~10 μW). In this case the photo current is generated by both SPP-photovoltaic effect (exciton generation) and direct injection of hot electrons coming from SPPs conversion (for details see S7). This term, reported in the inset of Fig. S10B, was straightforwardly obtained as I_{on} - I_{off}.

© 2013 Macmillan Publishers Limited. All rights reserved.

Limiting to the forward bias polarization range, the I_{off} *I–V* characteristic consists of an exponential part in the low current region and a resistance-limited part in the high current region. Based on the thermionic emission, the *I–V* characteristic of MS-type Schottky diode operated at $V > 3\ kT/q$ is described by the following equation:

$$I_F = S \cdot A^{**} T^2 \exp\left(\frac{q\Phi_{B0}}{KT}\right) \exp\left(\frac{q(V - I_F R_S)}{nKT}\right)$$

where I_F is the forward current, S is the area of Au contact, A^{**} is the effective Richardson constant (8 A cm^{-2} K^{-2} for GaAs n-type), T is the absolute temperature, K is the Boltzmann constant, q is the electron charge, ϕ_{B0} is the barrier height between Au and GaAs, n is the ideality factor, V is the applied voltage and R_s is the series resistance. By fitting the current equation to the measured *I–V* characteristics shown in figures S10A S11A and Fig.4b, the barrier height, ideality factor and series resistance can be extracted.

We point out that the measurements, both at the sub-gap and above the gap, were made in different point of the sample, founding consistency in the data reproducibility. Nevertheless, we noticed a local dependency of these measurements on the specific contact state and on the local chemistry, intrinsic to the sensitivity of the technique.

Figure S11 reports the representative *I-V* characteristics of our plasmonic structure when photoexcited at λ=980 nm by the incoming laser (laser power impinging on the grating ~10 μW). In this case the photo current is generated only by hot electrons transfer.

© 2013 **Macmillan Publishers Limited. All rights reserved.**

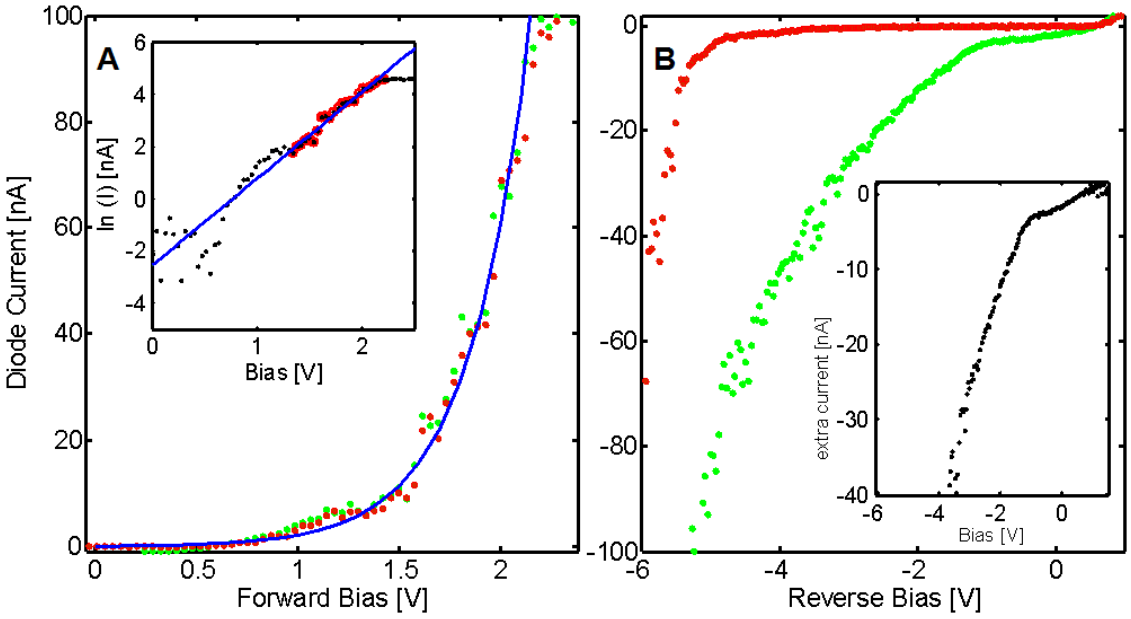

Fig. S10 *on* and *off* I-V characteristics of the nano sized Schottky junction for an exciting laser wavelength of 670 nm. **(A)** Forward bias. Green (I_{on}) and red (I_{off}) dots are the experimental determination while the blue line is the thermionic emission diffusion-model used to fit to experimental I_{off} data also reported in logaritmic scale in the inset. **(B)** Reversed bias. The two I-V characteristics show the two distinctive regimes. In the inset is reported the extra-current defined as I_{on}-I_{off} that we identify as the SPPs net current contributions, i.e. hot electrons plus SPP-photovoltage current due to the tip irradiation.

© 2013 **Macmillan Publishers Limited. All rights reserved.**

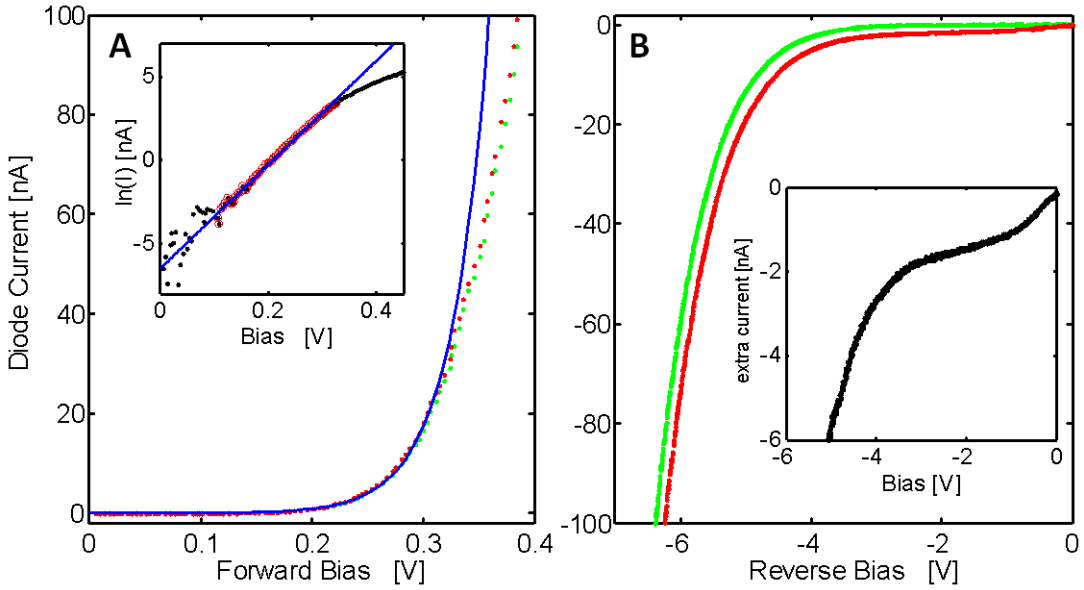

Fig. S11 *on* and *off* I-V characteristics of the nano sized Schottky junction for an exciting laser wavelength of 980 nm. **(A)** Forward bias. Red (I_{on}) and green (I_{off}) dots are the experimental determination while the blue line is the thermionic emission diffusion-model used to fit to experimental I_{off} data also reported in logarithmic scale in the inset. **(B)** Reversed bias. The two I-V characteristics show the two distinctive regimes. In the inset is reported the extra-current defined as I_{on}-I_{off} that we identify as the SPPs net current contributions, i.e. hot electrons trough the tip.

Parameter		value
R [nm]	Contact radius	6
S [nm^2]	Contact surface area	110
A** [Acm^{-2}K^{-2}]	Richardson constant	8
I_{TED} (qV>3KT)	$I_0 \exp(qV/nkT)$	
I_0 [nA]	$S A^{**}T^2 \exp(q\Phi_{B0}/KT)$	$2 \cdot 10^{-5}$
Φ_{B0} [V]	$KT/q \ln(SA^{**}T^2/I_0)$	0.43
n ideality factor	$q/kT \; dV/d\ln(I)$	4.8
V_{bi} [V]	$\Phi_m - \Phi_s$	0.66
V_{ON} [V]	Tip junction	1.6
V_{BD} [V]	Tip junction	-5.5
δ [nm]	Oxide layer thickness	0.7

Table S1 Electrical and band parameters measured and calculated for the Au/n-type GaAs Schottky tip junction of Fig. 4, Φ_m and Φ_s are the metal and semiconductor work functions. The corresponding *on* and *off* I-V characteristics (nano sized Schottky junction excited at laser wavelength of 980 nm) are described in the main text.

© 2013 Macmillan Publishers Limited. All rights reserved.

In Fig. S12A and B we report two unsaturated optical images of the device when illuminated with the 670 nm laser in out of contact condition. To clarify the coupling efficiency with respect to the relative orientation between the grating and the polarization direction of the incident radiation, the tip was placed on the focal plane of the objective to collect the scattered far field. Picture S12A demonstrates that radiation polarized along the tapered axis maximizes the photon to SPP conversion.

In Fig. S12C we report the linear dependence between photocurrent and optical power at 670 nm.

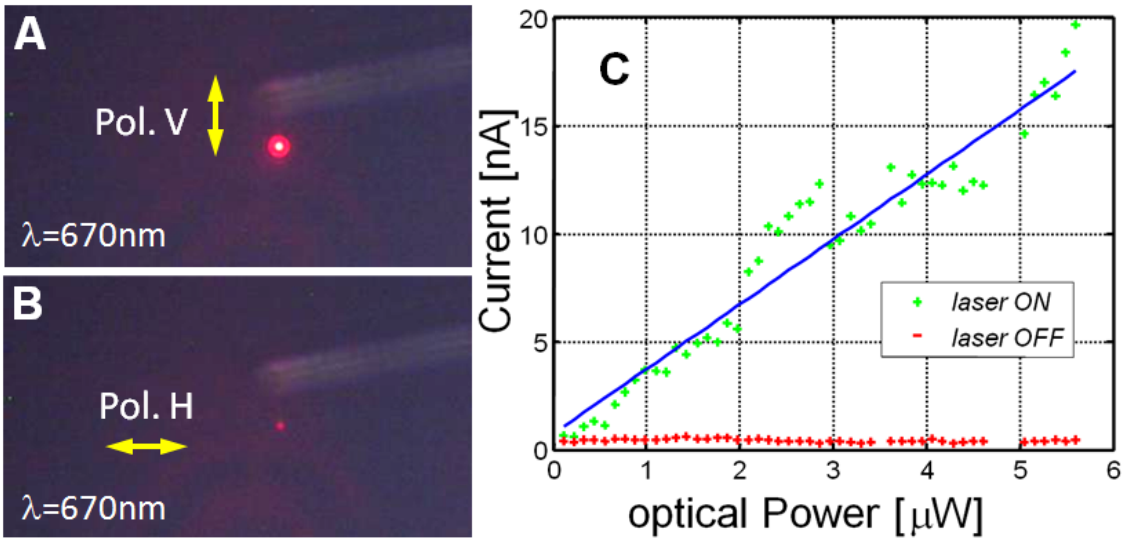

Fig. S12 (**A**) and (**B**) show typical tip emission in response to the two different polarization states of the incoming radiation, as indicated in the pictures. Out of plane defocusing effect, affecting the images acquired through the same illumination objective prevents to see clearly the whole AFM lever profile (**C**) Recorded current as function of the optical power demonstrating a linear dependence.

© 2013 **Macmillan Publishers Limited. All rights reserved.**

(S5) Evaluation of the contact area

In our experiment one of the most important parameters is the contact area between tip and substrate, which is critical to evaluate the photoelectrical properties of the nano Schottky contact. In order to evaluate the contact area we made direct measurements of the radius of curvature of several sample tips at nm level accuracy before and after IV measurements or surface scanning. This allowed us to optimize experimental parameters such as AFM force setpoint and laser power in order to have stable current signal for hours, good signal to noise ratio and minimal tip aging during measurements. In Figure S13 we report SEM images of two sample tips, before and after use in typical experiments (point contact IV characteristics and imaging measurements). By comparing these two images we could notice that only the tip used for contact mode imaging (5 nN load, 5 μm/s scanning speed, 2 hours continuous cycling, tip-sample bias of 1.5 V) on gallium arsenide substrate presents a modest flattening and wearing of the tip, while no appreciable plastic deformation could be observed for the force distance curve imaging case.

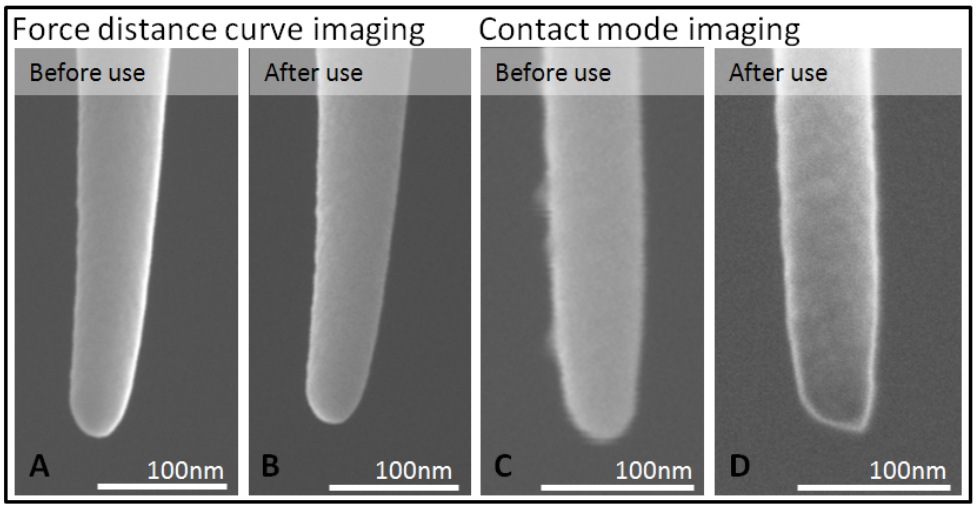

Fig. S13 Examples of tip shape before and after use with normal load, up to 5 nN. Absent or limited tip smear is found in case of force distance curve imaging (1000 curves) **(A), (B)** and for contact mode imaging **(C)** and **(D)** after two hour scanning with 5μm/s scanning speed and tip-sample bias of 1.5 Volt on gallium arsenide substrate.

© 2013 Macmillan Publishers Limited. All rights reserved.

Regarding the contact "footprint" of the tip on the sample, our estimation started from the radius of curvature of the tip, as explained in detail hereafter.

Atomic force microscopy is currently used for the evaluation of the local mechanical properties of samples thanks to its high force sensitivity. In this modality (our case) the tip interacts firmly with the surface during scanning and it can undergo elastic and plastic deformations that modify the tip profile. In the majority of the papers in literature that discuss this point, the Hertz model [10] has been tailored to describe the elastic deformation of contacting bodies, assuming that the materials are locally homogeneous and isotropic; the plastic deformation has been estimated comparing the maximum contact stress to the critical stress of the two material bodies [11].

In the presented experiments CSC38 AFM levers were adopted, characterized by a very low nominal spring constant k=0.03 N/m. From the "contact mode" force curve calibration (50 nN/Volt) and the set point (0.1 Volt) we estimated the contact force, about 5 nN, and the overall lever deflection from equilibrium position, ~160 nm see Fig. S15A. The cones were made of Pt-C, a hard compound, than coated by a gold layer 25 nm thick. Considering the elastic coefficients and Poisson ratios for the gold and for GaAs sample, respectively (78.5 N/mm^2, 0.42, and 85.5 N/mm^2, 0.32), we calculated the combined Young's modulus E_r of the tip and the sample system [12],

$$E_r = \left[\frac{\left(1-\nu_{tip}^2\right)}{E_{tip}} + \frac{\left(1-\nu_{sample}^2\right)}{E_{sample}} \right]^{-1}.$$

From this value (in the elastic Hertz model) we estimated the depth of indentation, the contact radius ~1.5 nm, and the maximum contact stress at the interface, $\sigma_{MAX,}$

$$\sigma_{MAX} = \left(\frac{6F_c E_r^2}{\pi^3 R^2} \right)^{1/3}.$$

© 2013 Macmillan Publishers Limited. All rights reserved.

All these values are reported as a function of the contact force in Fig. S14. Radius and contact area are to be considered as lower bound evaluations for the contact dimension that eventually can be maintained only for a single contact, and certainly not during regular scanning operations.

The other parameter, the critical stress for plastic deformation, was estimated as $\sigma_c \sim 0.6 \cdot H$, where H corresponds to the nanoscopic hardness, that we assumed to be in the same range of the bulk value (30 kg/mm^2 ~ 0.3 GPa). We did this assumption considering that, at the nanotip, at most one or few grains of gold were present (typical linear size of the order of 50nm), a fact that prevents the decrease in hardness, typical at the micro scale, due to the multiple grains rearrangement. (Poisson constants, $\boldsymbol{\nu}$, and Young's moduli, $\boldsymbol{E}$, and hardness, H, were from the CRC - Handbook Of Optical Materials 2003 [13]). The estimated critical stress for gold is about 0.2 GPa and about 6 GPa for the semiconductor, therefore it is reasonable to assume a flattening of the tip during the scanning until an equilibrium condition is reached. The process becomes much more evident if the scanning tip encounters a stepped surface. From these results, and considering also that the high aspect ratio of the cone certainly contributes to the damping, both elastically and plastically, of the local forces during the scanning, we are confident to estimate a contact operative radius in the range of $r_c = 6 \div 10$nm (contact area about 200 nm^2), see Fig.S14.

© 2013 Macmillan Publishers Limited. All rights reserved.

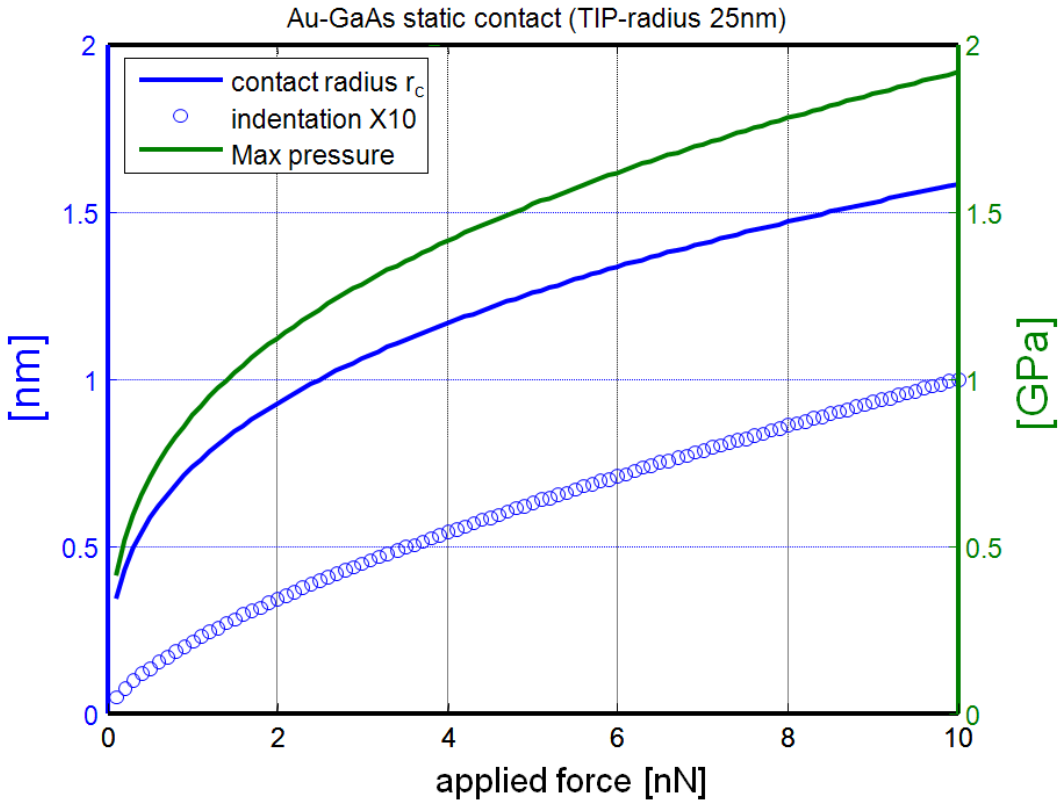

Fig. S14 Mechanical characterization of the tip-surface static contact. Contact radius, indentation depth and maximal pressure as function of the applied force (Hertz model).

© 2013 **Macmillan Publishers Limited. All rights reserved.**

(S6) Depletion region volume of a point contact Schottky diode.

It is known that doped GaAs has to be considered a partially (electrically) compensated semiconductor [14-15]. In particular, for Silicon dopant concentration higher that 10^{18} cm^{-3} the formation of neutral silicon pairs observed may lead to a progressive electrical deactivation of more than 85% of the silicon acceptors. This means that the free electron density is generally smaller than the amount of introduced dopant. The compensation in Si doped GaAs could, to some extent, be explained by simultaneous formation of donors and acceptors due to the amphoteric dopant incorporation. The degree of compensation, N_A/N_D, was found to be ~0.25 ÷ 0.3 at moderate doping levels regardless of the dopant kind. These considerations suggested us to determine the doping density, in agreement with literature experimental works [16-17], directly from the mobility and resistivity data known for our sample. We assumed a net carrier concentration $N_{e-} = N_D - N_A$ (free charge density) of ~$8 \cdot 10^{16}$ cm^{-3} and dopant density $N_d = N_D + N_A$, with averaged degree of compensation 0.275.

The downscale to nanometre size for a metal–semiconductor interface has gained enormous relevance in optoelectronics and it is one of the central themes in the modern material science applied to micro and nanoelectronics. The main result of diode downscaling in the atomic range is the no longer dependence of the thickness of the barrier on the doping level, but its dependence on size and shape of the junction itself [18]. This is particularly true if the diode size d is smaller than a characteristic length $L_c=(2\varepsilon_r\varepsilon_0(V_{bi}+V_{bias})/eN_{e-})^{1/2}$, ~106 nm for our case. L_c corresponds to the depletion length, W_d, only in the large scale case.

Furthermore, as the size of the semiconductor devices scales down, the traditional one-dimensional analysis of metal-semiconductor interface becomes completely inadequate and a three-dimensional model must be adopted [19-20] in order to explain the transport processes. Using the full depletion approximation, and assuming the space-charge-region homogeneously charged, the resulting free-boundary problem for Poisson's equation, where

© 2013 Macmillan Publishers Limited. All rights reserved.

the edge of the space-charge region is an unknown, can be approximately solved in oblate spheroidal coordinates [20]. As a rule, the metallic tip has to be described as a conductor at a given potential, nevertheless its charge (contact area per diode capacitance) results sufficiently localized at the nano-tip apex, and this allows it to be described as a point charge. In this sense, it is clear how the field lines spread out in the semiconductor roughly in a radial manner, while the isopotential surfaces describe a slightly prolate semispheroid. Additionally, the non uniform field results confined nearby the tip instead of extending smoothly as in *"large scale"* diodes, see Fig. S15.

In general, the full depletion approximation should be considered reasonably valid in the static problem and in moderate reverse bias condition, however it is not valid any longer in forward or strong reverse polarization of the junction, due to the expected screening effect of the free carrier crossing the depleted volume in proximity of the metal contact. In this case, space charge limited regime [21] could dominate the dynamic current performance, hence the current to voltage characteristics are expected to significantly depart from the ordinary behaviour.

Full depletion approximation framework assumes constant density and a sharp volume boundary, realistic only as long as the size of the volume is substantially larger than the Debye screening length scale, $L_D=(\varepsilon_r\varepsilon_0 KT/e^2N_{e^-})^{1/2}$, in our case ~15 nm. L_D represents the average distance necessary for the local electric field to modify (shielding action) the free charge density distribution.

Another inherent critical point of the generally accepted model derives from the assumption of a depletion region homogeneously charged, while in general the average distance among dopant atoms is $N_d^{-1/3}$. Randomly distributed dopants have a fundamental role in the determination of the Fermi level, hence on the contact potential. Our estimation for N_d is

© 2013 Macmillan Publishers Limited. All rights reserved.

~$1.15 \cdot 10^{17}$ cm^{-3}, thus $N_d^{-1/3}$ = 20 nm and $N_{e^-}^{-1/3}$ = 23 nm, resulting on the same scale size of the contact.

Assuming a contact radius r_c=8 nm (200 nm^2 area), the volume in which the potential halves its initial value contains roughly 28 doping atoms and only 20 free carrier. Consequently, when the discreteness of the charges in the depletion is considered, the potential landscape is no longer uniform, and every time a charged dopant results in proximity of the contact it locally modifies the potential, resulting in the distortion of the barrier shape. This effect increases the conduction of the diode, enhancing the tunnelling phenomenon, still maintaining the Schottky Barrier Height (SBH) substantially unaltered.

In contrast, hot electron injection from the metal to the semiconductor results less sensitive, being *h-e* current primarily sensible to the SBH itself, at least until the *h-e* energy ≥ SBH, as demonstrated in this work.

Numerical simulations of Ref. [18] offer a simple model to describe the barrier shape in small and large diodes and allowed us to calculate the depletion volume for our Schottky junction. The model shows that for $r_c << L_c$ the barrier thickness equals the diode size, i.e. for ultra small diode. In our case, we obtain a FWHM of the barrier width of 60 nm (Fig. S15C), indicating an important reduction of the depletion extension in respect to the planar case, as shown in Fig. S15B.

© 2013 **Macmillan Publishers Limited. All rights reserved.**

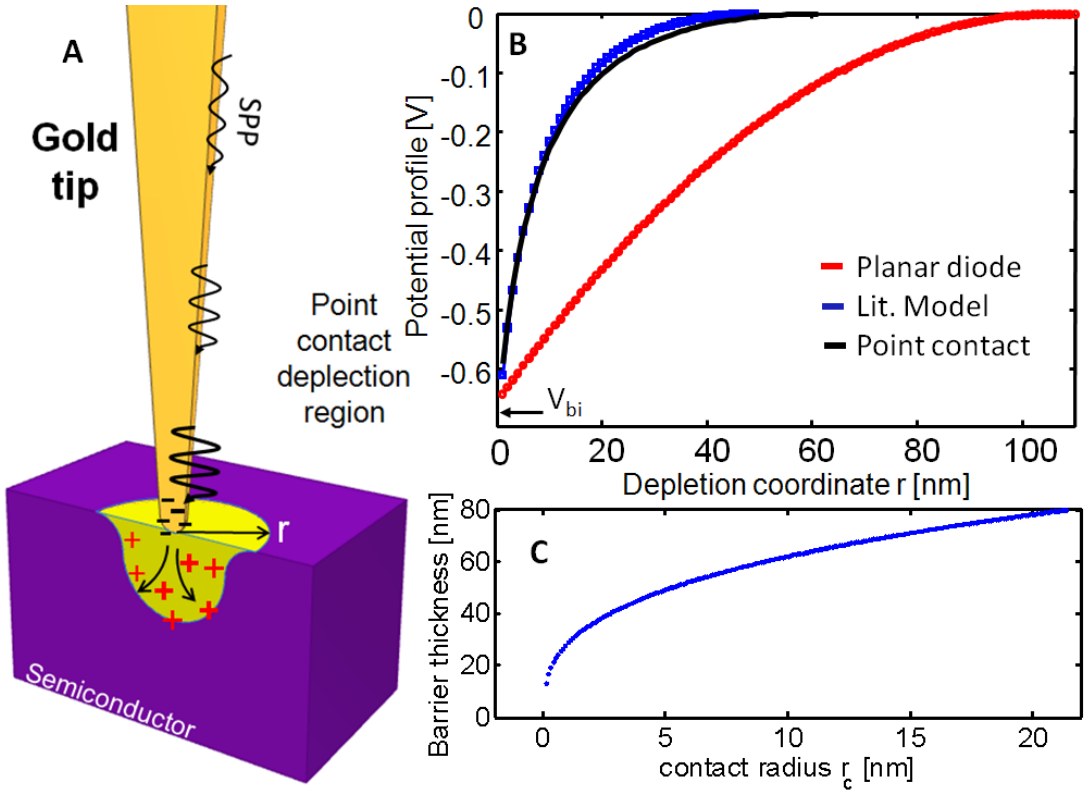

Fig. S15 Point contact geometry. **(A)** Sketch of the depletion region profile, E field radiate from the tip while isopotentials describe spheroidal surfaces. **(B)** Calculated potential inside the depleted volume for a planar diode (Red), model from Ref. [18] (Blu), and for a point contact geometry (Black) , for $N_{e^-} = 1.15 \cdot 10^{17}$ cm^{-3} and a contact radius of 8 nm (200 nm^2 area). In the calculation we considered an "half-space" N_{e^-} value equal to $N_{e^-}/2$ to compensate for the only half space extension of the actual semiconductor (the model considered adopts a spherical symmetric geometry: a metal contact embedded is a full space semiconductor). **(C)** Barrier thickness FWHM as function of the contact radius, for a point contact Schottky diode characterized by $N_{e^-} = 1.15 \cdot 10^{17}$ cm^{-3}.

© 2013 Macmillan Publishers Limited. All rights reserved.

(S7) Current terms that contribute to the detected photocurrent.

The first term is the tip to sample Thermionic Emission Diffusion current over the Schottky barrier, I_{TED}, [22] that for doping levels up to 10^{18} cm^{-3} is known to determine the current in a metal semiconductor planar junction (above this limit, tunnelling through the narrowed depletion layers dominates). Due to the particular geometry of the electrode (a point contact metal with nanoscale dimensions in contact with a n-type semiconductor), the I-V characteristic is accepted to depart from large scale behaviour [18], eventually it is expected to follow a Space Charge Limited (SCL) profile [21]. Furthermore, the I-V profile in metal semiconductor nano-contacts is alternatively explained either in terms of effective Schottky barrier height (a non-ideality parameter *n*, as defined in Fig. 4D), or in terms of surface minority carrier currents or enhanced tunnelling current from the semiconductor to the metal contact. The nanometric dimension of the contact modifies the depletion region extension, reducing it by a factor 2-3 in respect to the planar case, for the same doping level. Hence, the junction demonstrates a reduced resistivity; there is a partial shielding effect and a high electric field in the junction, which determines also an early onset for the avalanche breakdown effect. This current term can formally be expressed in a mathematical form as reported in table of Fig. 4D. Its contribution to the total photocurrent is exactly the I_{off} measured characteristic.

The second contribution is due to the photovoltaic effect, I_{PV}. It arises from the direct photo-generated electron-hole pairs (EHPs) into the semiconductor under direct laser illumination. For our setup it was a negligible contribution at every applied bias (light propagation is nearly paraxial to the surface, ~16°, focused within a Gaussian beam waist ≥4 μm at least 5 μm above the interested region). Furthermore, the EHP generation in the depletion region can be effective only if E_{photon}>Egap (1.42 eV) of the semiconductor, process

© 2013 Macmillan Publishers Limited. All rights reserved.

which is forbidden in the case of GaAs at λ=1060 nm (see also S10). Nevertheless, we estimated an upper bound for this term at λ=670 nm, considering the worst case, i.e. that light shines directly on the surface. Since EHPs can be generated and successfully collected only in the depleted volume we evaluated this volume (as a cylinder) starting from the depletion extension previously determined, ~60 nm (see Fig. S14B). Furthermore, we considered the absorption constant of the GaAs at the specific wavelength, α_{GaAs}(670 nm)=31000 cm^{-1} (corresponding to a penetration length ~320 nm), [23-24] and the transmission coefficient for TE polarized field at the incidence of 84° from the surface normal, about 0.05 (Fresnel refraction equations) , see Fig. S12C. Even assuming full laser intensity of 10 μW we obtain a current about 1 pA (8 pA for an 8-fold depletion volume corresponding at -3 V applied bias), more than three orders of magnitude lower than the one we measured.

The third contribution, I_{IPE}, is the classical internal photoemission at the metal semiconductor interface due to scattered laser illumination (the direct I_{IPE} can contribute to the measured current only if it occurs in the vicinity of the semiconductor at ~20 nm, i.e. on the length scale of the electron mean free path in the metal). The I_{IPE} can contribute to the measured current even without any applied bias. We could estimate the upper limit value for both these contributions by knowing the contact dimension (evaluating the depletion volume) and considering the maximum density of the e.m. field. In this case the absorption constant is α_{gold}(670 nm)=560000 cm^{-1} (corresponding to a penetration length ~15 nm), nevertheless the contribution is negligible for the same reasons given for the I_{PV} contribution.

The fourth contribution, $I_{SPP-IPE}$, is of the same kind of the third one, but it is due to the SPPs decay channel in hot electrons. In our experimental conditions, see Fig. S16B, the hot electron generation is particularly efficient due to the adiabatic transport of the SPPs to the apex of the cone (minimal energy loss up to the apex), where the SPPs are converted in

© 2013 Macmillan Publishers Limited. All rights reserved.

hot electrons with enhanced efficiency. The adiabatic cone ends abruptly with an apex on the same length scale as the electron mean free path. This confinement determines the effective damping of SPPs either in energetic electrons or in radiated photons.

The fifth contribution, $I_{SPP\text{-}PV}$, takes into account for the EHPs generated from the radiative decay channel of the SPPs scattered by the tip (that identifies the geometrical core of the depletion region), see Fig. S16B. This process, forbidden at λ=980 nm and λ=1060 nm for energetic consideration, results an intrinsically efficient tip assisted photovoltaic process when E_{photon}>Egap. At λ=670 nm, assuming a nearly unitary transmission into the semiconductor, we estimate some tens of nA for 1 μW of SSP integrally converted in photons, assumed the experimental condition reported in Fig. 6B.

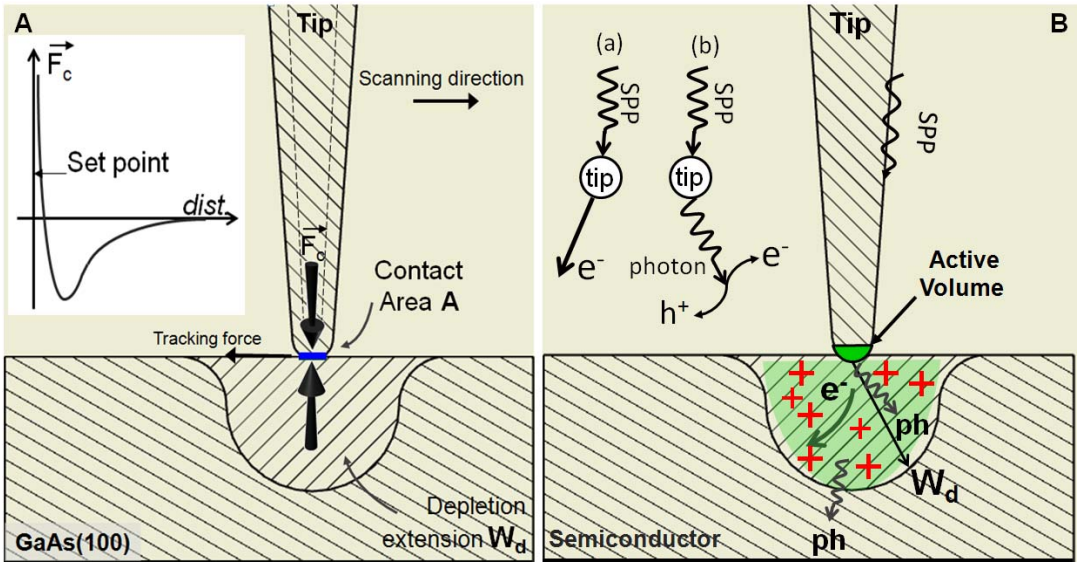

Fig. S16 Point contact geometry. (A) Illustration of the mechanical force balance of the tip-sample system. From the contact force F_c and the mechanical and geometrical characteristics of materials we estimate the contact surface area ~200 nm^2. (B) Sketch of the two relevant photo current contributions to the diode current: direct hot electron injection, $I_{SPP\text{-}IPE}$, and EHPs generated into the depleted volume, $I_{SPP\text{-}PV}$, active for E_{photon}>Egap.

© 2013 Macmillan Publishers Limited. All rights reserved.

(S8) Schottky Current in Adiabatic Concentrator

Here we introduce a specific model to treat hot electrons generation by adiabatic SPPs in the case of a conical geometry.

Optical (SPP) power $P(z)$ along the taper approximated as cylinder is

$$P(z) = P_0 \exp(-2k''z), \;\; k'' = \mathrm{Im}k\,, \tag{S1}$$

where k is a complex wave vector of the propagating SPPs. Consider a length Δz on the order of the electron mean free path, $\Delta z \sim 20$ nm. A change in the power at the this length is

$$\Delta P = -2k''P\,\Delta z\,. \tag{S2}$$

This decrease of the power is due to the decay of the SPPs into electron-hole pairs. Correspondingly, the number of hot electrons generated per unit time $\dot{N}$ (the generation rate) is

$$\dot{N} = 2k''\frac{P}{\hbar\omega}\,\Delta z\,, \tag{S3}$$

where ω is the SPP frequency. Note that for a taper thinner than the skin depth the dispersion relation can well be approximated analytically as

$$k = \frac{1}{R}\left[-\frac{\varepsilon_m}{2\varepsilon_d}\left(\ln\sqrt{-\frac{4\varepsilon_m}{\varepsilon_d}} - \gamma\right)\right]^{-1/2}, \tag{S4}$$

where R is the radius of the taper, ε_m and ε_d are the permittivities of the metal and dielectric respectively and $\gamma = 0.57721$ is the Euler constant. Probability η for a generated hot electron to pass over the Schottky barrier is

© 2013 Macmillan Publishers Limited. All rights reserved.

$$\eta = \frac{1}{2n}\int_0^{\pi/2} d\theta \sin\theta \int_0^{\varepsilon_F} d\varepsilon\, \rho(\varepsilon)\, \Theta\left[(\varepsilon + \hbar\omega)\cos^2\theta - (\varepsilon_F + e\phi_b)\right], \tag{S5}$$

where θ is an angle with respect to the normal to the junction plane where an electron is emitted, ε is the initial energy of the electron and $\rho(\varepsilon)$ is the density of states in the conduction band of the metal, ε_F is the Fermi energy, $e\phi_b$ is the height of the Schottky barrier (see Fig. 2C), and Θ is the Heaviside unit-step function. In deriving Eq. (S5), we assume that an electron is excited from any level of the conduction band of the metal with the same probability. We also assume that the hot electrons are generated isotropically; then only the energy $(\varepsilon + \hbar\omega)\cos^2\theta$ of the motion in the direction normal to the junction plane matters in comparison with Schottky barrier height. An extra factor of 2 in the denominator of the right-hand side of Eq. (S5) takes into account that only one half of all hot electrons propagate to the junction, and the second half is lost for the Schottky current. In Eq. (S5), n is the total number of the conduction electrons that can be excited by the decay of an SPP as limited by the conservation of energy and Pauli blocking principle,

$$n = \int_{\varepsilon_F - \hbar\omega}^{\varepsilon_F} d\varepsilon\, \rho(\varepsilon)\,. \tag{S6}$$

As determined by the Θ-function in Eq. (S5), the electron energy ε and the incidence angle θ change in the intervals given by the following inequalities

$$\varepsilon_F \geq \varepsilon \geq \frac{\varepsilon_F + e\phi_b}{\cos^2\theta} - \hbar\omega\,, \tag{S7}$$

$$1 \geq \cos^2\theta \geq \frac{\varepsilon_F + e\phi_b}{\varepsilon_F + \hbar\omega}\,. \tag{S8}$$

© 2013 Macmillan Publishers Limited. All rights reserved.

In the following, we take into account that $e\phi_b, \hbar\omega \ll \varepsilon_F$. Under these conditions, Eq. (S8) simplifies to

$$1 \geq \cos\theta \geq 1 - \frac{\hbar\omega - e\phi_b}{2\varepsilon_F}. \tag{S9}$$

Also, the density of states in Eq. (S5) can be taken at the Fermi surface, i.e. we can set $\rho(\varepsilon) \approx \rho(\varepsilon_F)$. Taking this result and Eqs. (S7) and (S9) into account, we can rewrite Eq. (S5) as

$$\eta = \frac{1}{2n} \int\limits_{1-\frac{\hbar\omega - e\phi_b}{2\varepsilon_F}}^{1} d\cos\theta \int\limits_{\frac{\varepsilon_F + e\phi_b}{\cos^2\theta} - \hbar\omega}^{\varepsilon_F} d\varepsilon\,. \tag{S10}$$

Also Eq. (S7) becomes

$$n = \rho(\varepsilon_F)\hbar\omega\,. \tag{S11}$$

Integration of Eq. (S10) is elementary, and we immediately get the efficiency of the electron collection by the Schottky junction as

$$\eta = \frac{(\hbar\omega - e\phi_b)^2}{4\varepsilon_F \hbar\omega} \cdot \Theta\,[\hbar\omega - e\phi_b], \tag{S12}$$

Note that $\eta \ll 1$, and the quadratic dependence on the excess of the maximum electron energy over the barrier, $\propto (\hbar\omega - e\phi_b)^2$ is the same as in the well-known Fowler formula [25], see also [26]. Finally, the Schottky-junction current is

$$J = e\eta\dot{N}\,, \tag{S13}$$

where the hot-electron generation rate $\dot{N}$ is given by Eq. (S3).

© 2013 Macmillan Publishers Limited. All rights reserved.

In the case if an excited electron is scattered at the interface and the momentum conservation is, therefore, relaxed, instead of Eq. (S5) we have

$$\eta = \frac{1}{2n}\int_0^{\pi/2} d\theta \sin\theta \int_0^{\varepsilon_F} d\varepsilon \rho(\varepsilon)\Theta\left[\varepsilon + \hbar\omega - \left(\varepsilon_F + e\Phi_b\right)\right]. \tag{S14}$$

The integration now is trivial, and we obtain

$$\eta = \frac{\hbar\omega - e\Phi_b}{2\hbar\omega} \cdot \Theta\left[\hbar\omega - e\Phi_b\right], \tag{S15}$$

which is a much greater value than that of Eq. (S12) since .

Parameter		GaAs (λ_1=670nm)	GaAs (λ_2=980nm)	GaAs (λ_3=1060nm)
R tip radius	[nm]	25nm		
Coupled power	[μW]	1 (as after 10% coupling)		
χ_s (electron affinity)	[V]	4.68		
Φ_m (gold workfuntion)	[V]	5.1		
E_F (gold Fermi Energy)	[eV]	4.8		
Φ_B (contact barrier)	[V]	0.42		
η transfer efficiency (eq.1)	%	6	2.9	2.5
Responsivity (eq.1,3)	[nA/μW)]	1.4	0.29	0.2
η transfer efficiency (eq.2)	%	38	33	31
Responsivity (eq.2,3)	[nA/μW)]	9.7	3.3	3.1

Table S2 | SPP-to-hot-electron conversion efficiency and responsivity. Conversion efficiency η and responsivity ρ for the n-type GaAs Au-tip Schottky junction presented in the main text for the three wavelengths, calculated with relation eq.1 (S12) and eq.2 (S15), and eq.(3).

© 2013 Macmillan Publishers Limited. All rights reserved.

(S9) Evaluation of maximum temperature increase

In order to address the effects that temperature might have on the current generation, we have numerically calculated the maximum temperature increase that the metallic tip can experience under our experimental conditions. To do so, we have coupled Maxwell's equations with Joule's equation, and conduction heat transfer was taken into account. Intentionally we overestimated the experimental input parameters by considering the whole incidence laser power P=10 μW to be dissipated in a small volume close to the tip Au/GaAs interface. In fact, from an experimental point of view, this means assuming 100% coupling between the incident light (10 μW) and the grating together with no dissipation of the surface plasmon polaritons along the path from the grating to the tip. The numerical calculations were carried out using the Finite Element Method. We want to stress that 10μW is by far more than the actual dissipated power by the device even considering the DC power dissipation due to hot electrons current. This last contribute has been in fact proven to be negligible for the measured values of current [27-28].

The simulation was accomplished considering a spherical domain (r = 2.5 nm) embedded at the end of the tip at 5 nm from the Au/GaAs interface, since this is the region where we expect most of the dissipation by the system (Fig. S17). This domain was set as a 10 μW heat source.

© 2013 Macmillan Publishers Limited. All rights reserved.

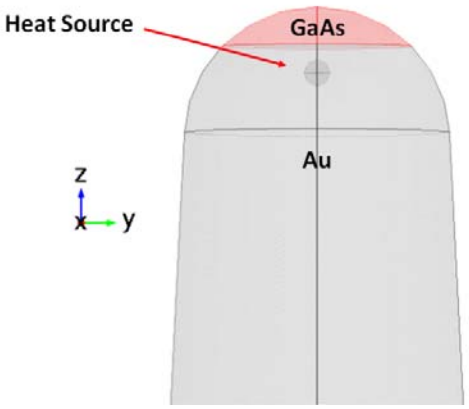

Fig. S17 Heating modelling: a spherical domain (r=2.5 nm) has been embedded below the Au/GaAs interface at 5 nm from the GaAs surface. Dissipating power was set at P=10 μW. The interface between the Au and the GaAs represents the contact area.

The base of the cone (2.5 μm away from the heat source) was kept at fixed room temperature (T_0=293.15 K) to reproduce a very high thermal capacity which in reality corresponds to the whole cantilever used in the experiment. In a similar way the bulk GaAs region was considered as an 800 nm thick spherical cap (2.2 μm of radius) whose external surface was again fixed at T_0 as shown in Fig. S18:

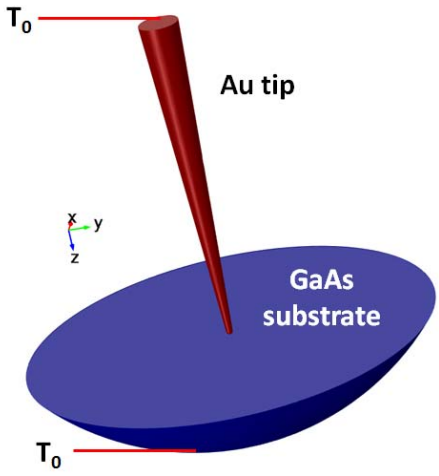

Fig. S18 Simulation geometry: the tip has been put in contact with a 800 nm GaAs spherical cap (R=2.2 μm). In order to replicate the thermal boundary condition of the experimental

© 2013 Macmillan Publishers Limited. All rights reserved.

system, both the base of the Au tip and the GaAs cap outer surface have been fixed at T_0=293.15 K.

The numerical calculations resulted in a maximum increase of the temperature of about 4 K mainly localized where the heating was generated. In Fig. S19 we show the plot of the temperature along a 200 nm line centred in the heating domain and parallel to the conical tip axis:

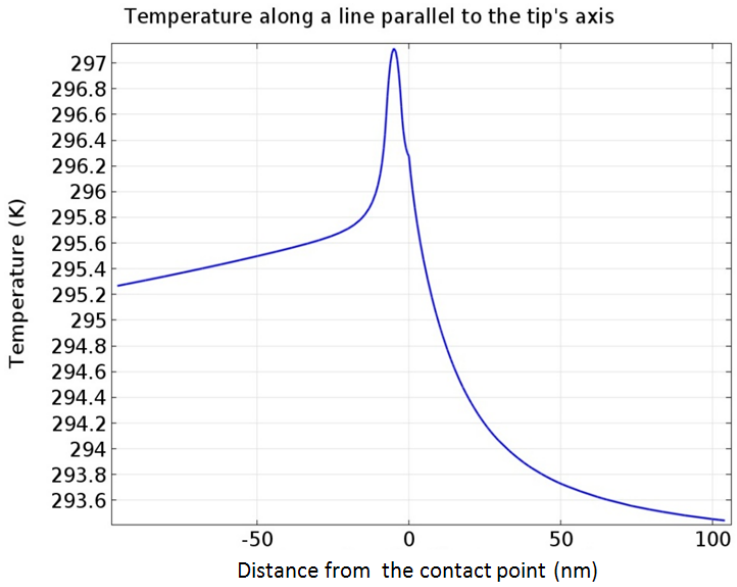

Fig. S19 Temperature profile: temperature values have been plotted along a line (L=200 nm) parallel to the cone axis centred on the heating domain. The maximum temperature (about 297 K) is reached in the heating domain. The small hump at the right of the peak is due to the Au/GaAs interface where thermal parameters change for the two materials.

As expected, the maximum temperature (less than 300 K) is reached in the centre of the heating domain. At distances of 100 nm in both directions, temperature increase is very low: about 2 K for Au and negligible for GaAs. This result is consistent with those previously reported by Parkhi and Gross[27]. The small feature at the right of the peak in correspondence

© 2013 Macmillan Publishers Limited. All rights reserved.

to 0 nm position is due to the Au/GaAs interface where thermal characteristics change. We report also the height profile temperature map on the YZ plane of the structure near the interface (Fig. S20):

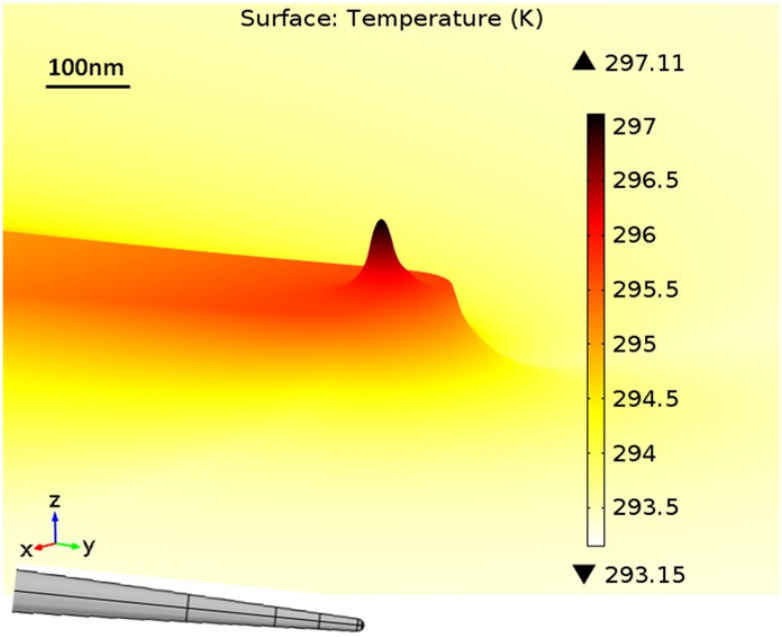

Fig. S20 Temperature map: height profile of the temperature reached in the upper part of the tip, across the Au/GaAs interface.

Finally, we observe that temperature quickly decreases in all directions and its maximum value cannot be considered high enough to trigger any temperature-dependent structural change. Considering gold thermal expansion ($45*10^{-6}$ K^{-1}) a 2 K temperature increment produce a +0.1nm per 1micron length, not affecting our measurement.

© 2013 **Macmillan Publishers Limited. All rights reserved.**

S10 Photoluminescence (PL) and Absorption (ABS) characterization of GaAs sample.

We have studied the carrier concentration in the Si doped (*n*-type) GaAs sample investigated in the paper, using photoluminescence (PL) spectral measurement. Owing to its optical nature, PL gives the advantage of a contactless characterization differently from other techniques such as Hall measurements. Due to the amphoteric nature of Si as dopant in GaAs semiconductor, the Si donors could be partially compensated by various acceptors in the growth process with a ratio that depends from the dopant concentration itself, therefore the final electron concentration is normally lower than the nominal Si doping level, and it is fruitfully determined via one direct measurement technique rather than retrieved via the dopant concentration.

It is known that for n-type semiconductors both the lineshape and the position of the PL peak sensibly depend on the electron concentration; in particular the principal PL peak broadens and shifts to higher energy as the electron concentration increases, even if a general band-gap narrowing is observed. This is explained considering that the emission band extends from the reduced band-gap energy, which is the difference between the top of the valence band and the bottom of the conduction band, to the energy of the optical absorption gap, which is determined by the band filling [29]. The PL experiment was performed at room temperature using a 520 nm excitation on a HORIBA Scientific FluoroMax® system, and the resulting spontaneous emission spectrum is presented in Fig. S21A. In respect to the peak at 1.424 eV (36 meV FWHM) usually observable for the undoped GaAs material at 300 K, corresponding to the known band-gap transition of the GaAs material, the PL spectral peak of our Si-doped GaAs material appears blue-shifted to 1.480eV and broadened 40 meV FWHM, which is in agreement with literature data for the doped material [30-31]. The PL features appearing at the low energy side of the GaAs peak are usually related to impurity band recombination.

© 2013 **Macmillan Publishers Limited. All rights reserved.**

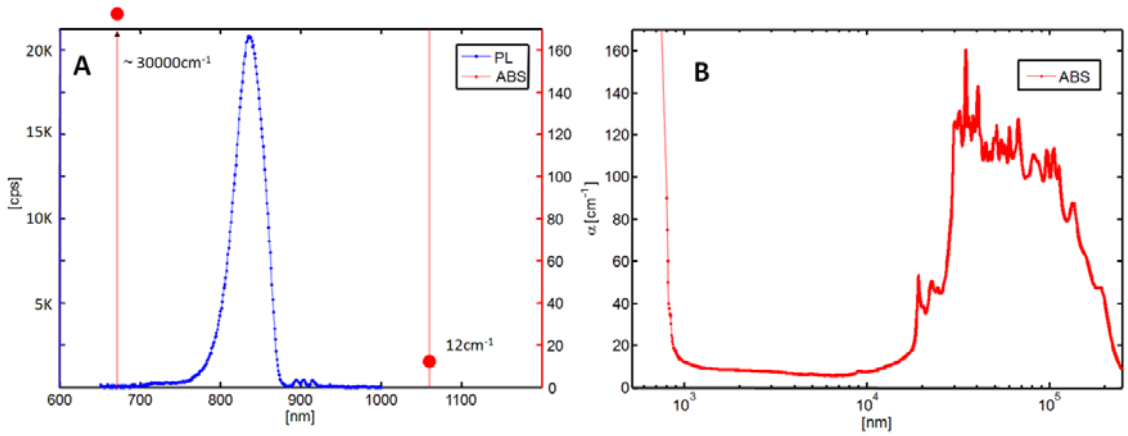

Fig. S21 (A) Spontaneous emission spectrum for the doped n-GaAs sample at 300 K. Red marks are the measured absorption coefficient values extracted from image **(B)**. **(B)** Absorption coefficient, α [cm^{-1}], for the n-type GaAs sample at 300 K. Single or multi-phonons absorption processes are responsible for the low frequency spectral profile features.

In figure S21B the absorption coefficient values measured for our sample at 1060nm and at 670 nm [23] are also reported. We can notice that at 1060 nm a very low absorption coefficient (12 cm^{-1}) is found when compared with the band edge value of 8000 cm^{-1} and the absorption coefficient at 670 nm (30000cm^{-1}).

From these results, also considering ref.32 and for the considerations introduced in S7, a negligible photocurrent contribution is expected (the sample is roughly transparent with an absorption length of ~800 μm, and the small features observable between 880 nm and 930 nm cannot induce any effective excitation at 980 nm and 1060 nm). The measured absorption coefficient at 1060nm allows us to evaluate directly the PV terms, both in the expected case of emission from the tip and in case of accidental illumination of the depleted region due to laser light. For 1 μW ($5.3*10^{12}$ photons @1060 nm), considering an extension of the depleted region of 100 nm, we obtain a detectable current of just ~6 pA and ~10 fA respectively, considering a spot diameter of 2 μm. Both these values are definitely below the measured current.

© 2013 Macmillan Publishers Limited. All rights reserved.

(S11) I-V characteristic of a n-type Si/Au point contact Schottky diode and control experiments.

To characterize the plasmonic properties of the Si/Au device we used the same methodology adopted for the case of GaAs. In the present situation the semiconductor was a moderately doped n-type silicon (111) sample (phosphorus doped, 10÷25 Ωcm ≈ $5*10^{14}$ e^-/cm^3), freshly etched in a 2% HF solution for 3min in order to remove the native oxide layer. A dual gain trans-impedance amplifying circuit recorded the currents from the sample within the range 10 pA ÷ 10 μA while the biasing voltage was applied directly to the sample. A homemade optical system provided the tip surface illumination with a Gaussian beam, at an incidence angle of 36° from the normal to the grating surface, see Fig. S8. The spot size produced a uniform illumination of the pyramidal area. All the measurements were performed in tip-sample contact (AFM contact mode) while a dried nitrogen constant flux into the AFM chamber was allowed to partially reduce both, the humidity around the sample, and the rapid oxidation process normally observed for freshly etched Si samples employed for conductive AFM applications. The photo excitation was stimulated by a vertically polarized single mode laser at λ=670 nm (1.85 eV), higher than the 0.9 eV Au-Si Schottky barrier and the semiconductor band gap, about 1.45 eV.

© 2013 Macmillan Publishers Limited. All rights reserved.

Figure S22 shows a temporal interval of the acquired current profile, while Fig. S23 refers to the two current-to-voltage characteristics. The SPPs photocurrent contribution (black line) obtained as I_{ON}-I_{OFF} is also reported.

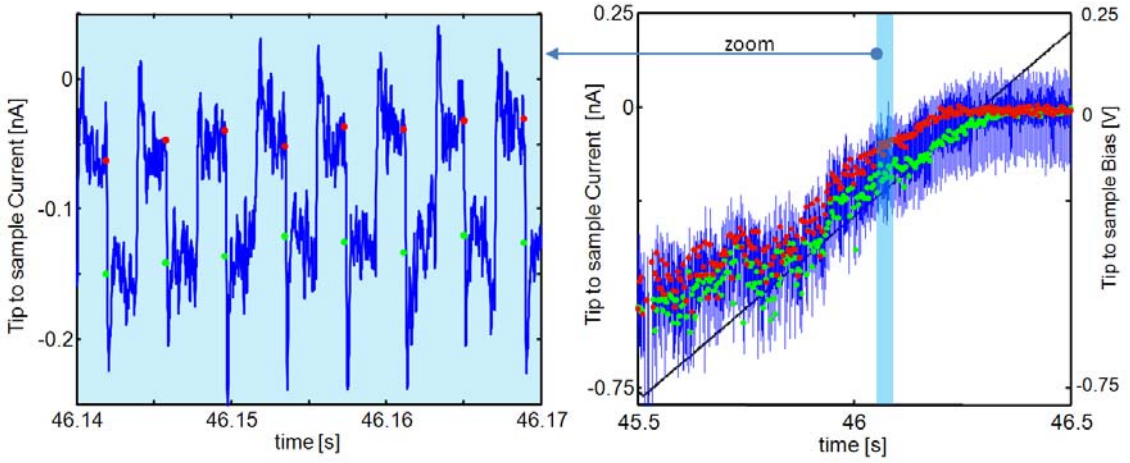

Fig. S22 The picture shows the temporal profile (blue data) of the acquired current-to-voltage characteristic (sampling rate of 100 kHz) for an exciting laser wavelength of 670 nm while a voltage bias ramp was applied (1 Vpp black line). For each optical cycle data subsets, unaffected by the transient process, were identified. Each single interval was then averaged to obtain a couple of numbers, one for each cycle (green and red points in the picture), identifying the actual values of the current both under illumination and in dark condition at the corresponding bias voltage value.

© 2013 **Macmillan Publishers Limited. All rights reserved.**

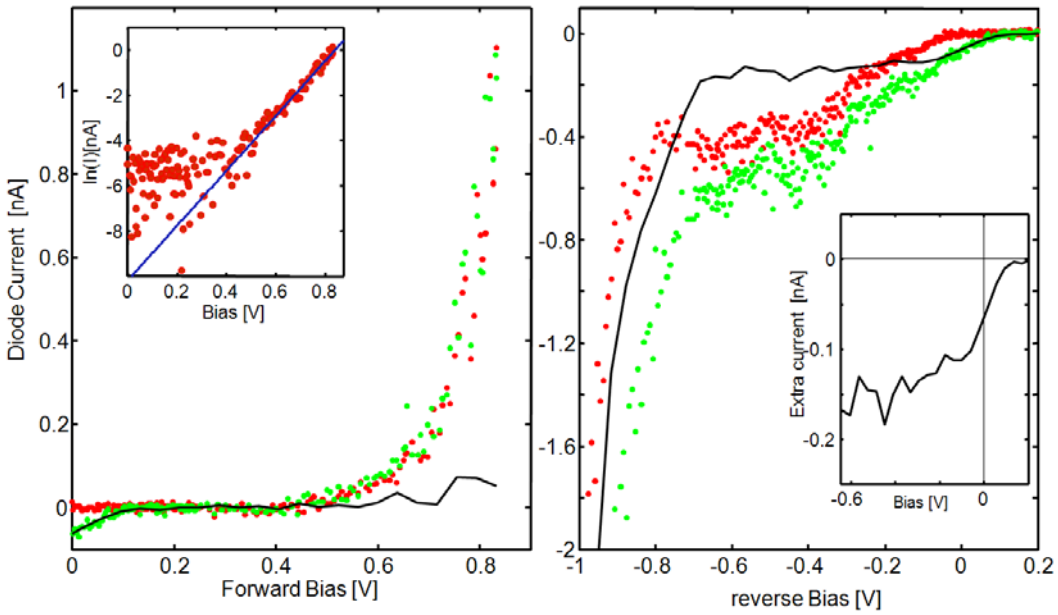

Fig. S23 *on* and *off* I-V characteristics of the nano sized Schottky junction for an exciting laser wavelength of 670 nm. Green (I_{on}) and red (I_{off}) dots are the experimental determination, as described in S3. (A) Forward bias. The blue line in the inset is the thermionic emission-diffusion model used to fit the experimental I_{off} data. (B) Reversed bias. In the inset is reported the extra-current defined as I_{on}-I_{off} that we identify as the SPPs net current contributions.

Growing oxide layer on silicon.

In Fig. S24 we report about the current reduction phenomenon observed many times in the characterization of the tip-semiconductor junctions. It was observable during the I-V acquisition and it was particularly effective for the Si sample, in respect to the GaAs sample case; We explained this behavior considering that our device works in standard STP conditions, i.e. temperature and humidity typical of laboratories. In fact, in these conditions the growth of silicon oxide directly under the tip can be expected and observed normally, with an increased rate due to the current flow process itself. The oxide layer acts as a potential barrier for the electrons flux that shifts progressively the conductive onset voltage to lower or higher values. A constant N2 flux introduced in correspondence of the AFM head

© 2013 Macmillan Publishers Limited. All rights reserved.

partially diminishes the humidity on the tip-surface contact, thus reducing the conductive-AFM oxidation rate that, otherwise, would take place at the microsecond time scale. For the reported experimental conditions we evaluate a characteristic timescale of about 3sec.

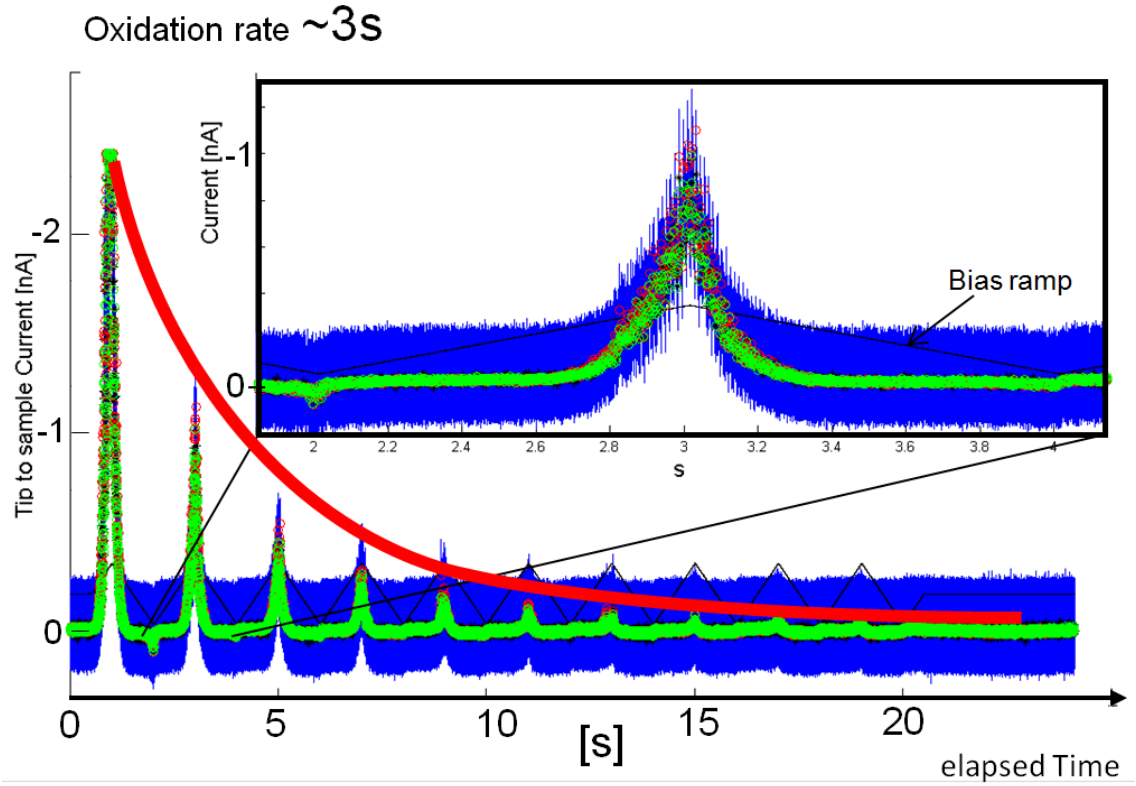

Fig. S24 Au/n-type Si nano-junction current profile. Blue line is the temporal evolution of the acquired signal, green and red circles are the experimental determination of I_{on} and I_{off}, as described in S3, while the black line is the applied voltage bias ramp. The rapid reduction of the current is due to an oxidative process occurring at the tip sample interface.

In support of this explanation we list these experimental considerations:

1) Our best results were obtained for samples just after the etching procedure in a 2% HF solution for 3min, and with a tip in pristine conditions.
2) By moving the point contact to a second different position on the sample surface, renewed conditions could be re-established.

© 2013 Macmillan Publishers Limited. All rights reserved.

3) The consecutively acquired IV characteristics, as measured for increasing steps of the applied potential amplitude, tend to shift toward negative bias values, rather than revealing new contributes to the IV profile.
4) Typically an oxide interfacial layer is expected to increase the built-in potential (as it can be seen with a C-V measurement) and decreases the internal potential across the semiconductor, which increases the measured ideality factor and saturation current. It also limits the maximum current density.

From experimental point of view, the use of Silicon is not the best choice for a *proof of concept,* due to the surface sensitivity to environmental conditions. This is one of the reasons that guided us to use GaAs surface, very stable, by which we could stably show the role of hot electrons.

On the contrary, the "instabilities" with silicon is also a proof of local chemical sensitivity that, in case of silicon, has a time scale well below the second.

(Control Experiment #1) TIP – grating less.

A first control experiment was accomplished with no grating engraved on the cantilever pyramid. No current generation and light scattering was measured in the experiment, as expected. This clearly demonstrates that the residual roughness on the gold surface (less than 1 nm) could not act as momentum matching between the photon and plasmon.

(Control Experiment #2) TIP – Cr coated.

Less trivially, we also report the photoconduction property of a Cr coated device placed in contact with the Silicon sample (Cr/n-Si SB height ~0.6 eV) for an applied saw tooth ramp up to +/-5 V. Chromium can be considered a non plasmonic metal since it is characterized by a greatly reduced SPP propagation length at the experimental laser wavelength of 670 nm, in respect to gold or silver. As expected, no significant extra-current was detected for Cr coated device (sputtered with a 25 nm chromium layer) when illuminated with laser power up to 50 μW (see Fig. S25A, B).

© 2013 **Macmillan Publishers Limited. All rights reserved.**

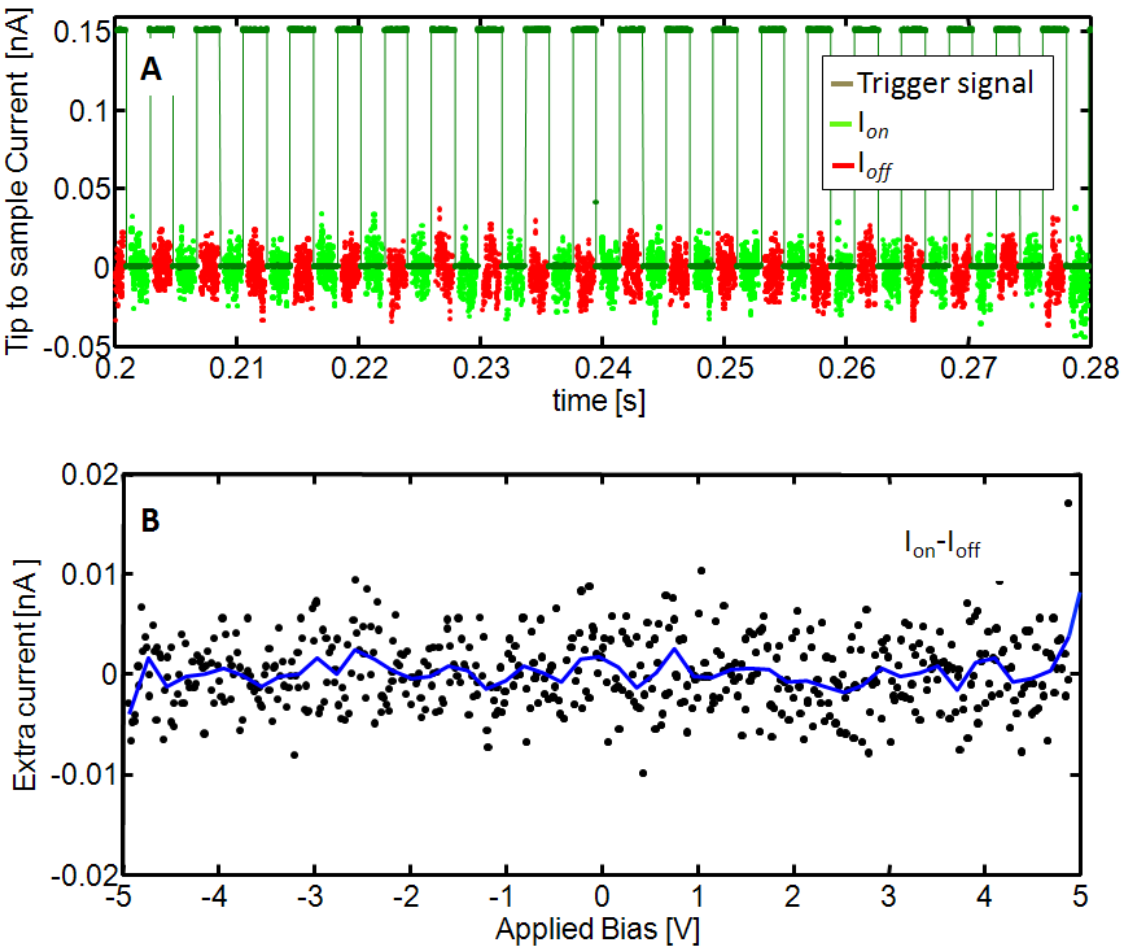

Fig. S25 (A) on/off current temporal profile acquired for an exciting laser wavelength of 670 nm, and trigger monitor of the laser (TTL-green signal). For each optical cycle data subsets, unaffected by the transient process (green and red points in the picture), were identified. **(B)** Extra-current obtained from the I-V characteristics recorded (I_{on}-I_{off}) applying saw tooth ramps up to +-5 V ramps.

© 2013 **Macmillan Publishers Limited. All rights reserved.**

(Control Experiment #3) Uncoated Silicon Tip (n-type)

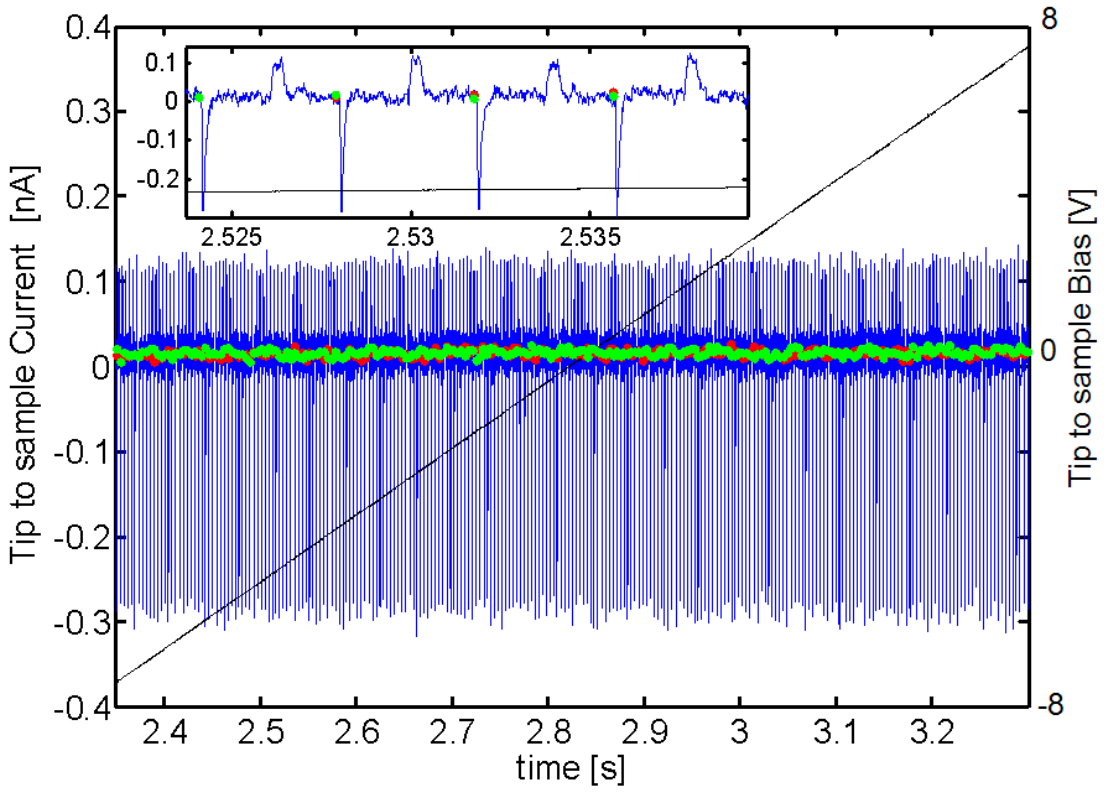

Fig. S26 The current signals recorded with the photocurrent AFM set-up at 670 nm for the uncoated tip show only current transient effects, due to majority carrier trapping and no net current dependence by the laser power.

It is known that a photon with energy $h\nu > E_{gap}$ can be easily absorbed by a semiconductor since its valence band contains many electrons, while the conduction band has many empty states into which the electrons may be excited. Initially, these electrons may have more energy than the typical electrons belonging to the conduction band, thus they will tend to release energy to the lattice through scattering processes until their velocity reaches the thermal equilibrium. Since these extra carriers are out of balance with their environment, they must recombine (ex. photoluminescence or heat), until they are in condition to contribute to the conductivity of the material.

© 2013 Macmillan Publishers Limited. All rights reserved.

However, in silicon the vast majority of the recombination events happen indirectly via recombination levels within the band gap, and the energy loss resulting by electron recombination is usually transferred up to the lattice as heat rather than by emission of photons. This is a well known two steps process (hole capture and subsequently electron capture). As result the recombination centres (or local traps) give rise to a variation of the sample conductivity with a time scale of some tens of microseconds. The temporal evolution of the photoexcitation event can be described in terms of current transients and steady states, as:

- Current transient: electron-hole pairs are photo generated under illumination in a characteristic time scale of few nanoseconds, determining an instantaneous out of equilibrium condition for the density carriers in the semiconductor. Two phenomena concur to reach the new equilibrium condition (under illumination steady state): the first one, occurring just below the silicon surface, is the instantaneous trapping by free traps or impurities of a part of the generated photo-curriers (i.e. one of the two species generated is trapped while the other one is free to flow to the electrode), thus determining a net current initial peak. The second is the slow recombination process of EHP that, in silicon, is an indirect process. This is characterized by a timescale of 2 microseconds for a doping level of 10^{18} donors. The observed value of $\sim 10^2$ μs can be addressed to the thermal relaxation time of the tip, mainly due to the phonons propagation.

- Steady state: the illuminated steady state is characterized by the balance of the optical pumping and the EHP recombination process into the semiconductor.

This phenomenon, as we have observed, is an indirect process for silicon, characterized by a net energy transfer to the lattice that thermalizes thus determining a net heating of the sample. During this steady state small quantities of charge contribute to the current, however these

© 2013 Macmillan Publishers Limited. All rights reserved.

values are under our sensitivity level. When the illumination is turned off the system gets again out of the equilibrium and photo trapped carriers are free to move back, generating a net current peak.

With these considerations we can then understand the transient peaks in the current profile observable in Fig. S26.

Supplementary References

1. http://www.comsol.com/products/multiphysics/.
2. Rakic, A. D., Djurisic, A. B., Elazar, J. M. & Majewski, M. L. Optical Properties of Metallic Films for Vertical-Cavity Optoelectronic Devices. *Appl. Opt.* **37**, 5271-5283 (1998).
3. Ritchie, R. H., Arakawa, E. T., Cowan, J. J. & Hamm, R. N. Surface-Plasmon Resonance Effect in Grating Diffraction. *Physical review letters* **21**, 1530-1533 (1968).
4. Lalanne, P., Hugonin, J. P. & Rodier, J. C. Theory of Surface Plasmon Generation at Nanoslit Apertures. *Physical review letters* **95**, 263902 (2005).

© 2013 **Macmillan Publishers Limited. All rights reserved.**

5. http://www.cst.com/.
6. Proietti Zaccaria, R. *et al.* Surface plasmon polariton compression through radially and linearly polarized source. *Optics Letters* **37**, 545-547 (2012).
7. Proietti Zaccaria, R. *et al.* Fully analytical description of adiabatic compression in dissipative polaritonic structures. *Phys. Rev. B* **86**, 035410 (2012).
8. Moretti, M. *et al.* Reflection-mode TERS on Insulin Amyloid Fibrils with Top-Visual AFM Probes. *Plasmonics*, 1-9, (2012).
9. M. Lorenzoni, B. Torre Scanning probe oxidation of SiC, fabrication possibilities and kinetics considerations. APL 103, DOI: 10.1063/1.4825265 (2013).
10. Hertz, H. Ueber den kontakt elastischer koerper. *Journal für die reine und angewandte Mathematik* **92**, 15 (1881).
11. Bloo, M. L., Haitjema, H. & Pril, W. O. Deformation and wear of pyramidal, silicon-nitride AFM tips scanning micrometre-size features in contact mode. *Measurement* **25**, 203-211, (1999).
12. Khurshudov, A., Kato, K. & Koide, H. Nano-wear of the diamond AFM probing tip under scratching of silicon, studied by AFM. *Tribol Lett* **2**, 345-354, (1996).
13. Weber, M. J. *Handbook of optical materials*. (CRC Press, 2003).
14. Ketterer, B., Mikheev, E., Uccelli, E. & Fontcuberta i Morral, A. Compensation mechanism in silicon-doped gallium arsenide nanowires. *Applied Physics Letters* **97**, 223103-223103 (2010).
15. Hilse, M., Ramsteiner, M., Breuer, S., Geelhaar, L. & Riechert, H. Incorporation of the dopants Si and Be into GaAs nanowires. *Applied Physics Letters* **96**, 193104-193103 (2010).
16. Tang, X. *et al.* Si-doping of MOCVD GaAs: Closer analysis of the incorporation process. *Journal of Crystal Growth* **98**, 827-837 (1989).
17. Venkatasubramanian, R., Patel, K. & Ghandhi, S. K. Compensation mechanisms in n+-GaAs doped with silicon. *Journal of Crystal Growth* **94**, 34-40, (1989).
18. Smit, G. D. J., Rogge, S. & Klapwijk, T. M. Scaling of nano-Schottky-diodes. *Applied Physics Letters* **81**, 3852-3854 (2002).
19. Donolato, C. Electrostatic problem of a point-charge in the presence of a semiinfinite semiconductor. *Journal of Applied Physics* **78**, 684-690 (1995).
20. Donolato, C. Approximate analytical solution to the space charge problem in nanosized Schottky diodes. *Journal of Applied Physics* **95**, 2184-2186 (2004).

© 2013 **Macmillan Publishers Limited. All rights reserved.**

21. Lampert, M. A., Many, A. & Mark, P. Space-Charge-Limited Currents Injected from a Point Contact. *Physical Review* **135**, A1444-A1453 (1964).
22. Simon M. Sze, K. K. N. *Physics of Semiconductor Devices - Third Edition* (Hoboken, N.J. : Wiley-Interscience, ©2007., 2006).
23. http://refractiveindex.info/. *GaAs refractive index*,
a. <http://refractiveindex.info/?group=CRYSTALS&material=GaAs> (2012).
24. H. C. Casey, J., D. D. Sell, and K. W. Wecht. *J. Appl. Phys.* **46** (1975).
25. Fowler, R. H. *Phys. Rev.* **38**, 45 (1931). Palik, E. D. Handbook of optical constants of solids. Part II., (Academic Press, 1985).
26. Sze, S. M. *Physics of semiconductor devices*. 3rd ed. edn, (Wiley-Interscience, 2007)
27. Parkhi, A. & Gross, T. S. Impact of I-V behavior and estimated temperature rise on surface and tip modification of the nanocontact between a highly doped silicon scanning probe microscope tip and gold surface under ambient conditions. *Journal of Applied Physics* **109**, 014323-014327 (2011).
28. Huber, R., Koch, M. & Feldmann, J. Laser-induced thermal expansion of a scanning tunneling microscope tip measured with an atomic force microscope cantilever. *Applied Physics Letters* **73**, 2521-2523 (1998).
29. Van Mieghem, P., Mertens, R. P., Borghs, G. & Van Overstraeten, R. J. Band-gap narrowing in GaAs using a capacitance method. *Physical Review B* **41**, 5952-5959 (1990).
30. Young-Ki Ha, C. L., Jae-Eun Kim and Hae Yong Park. Defect Luminescence in Heavily Si-Doped n- and p-type GaAs. *Journal of the Korean Physical Society* **36**, 42-48 (2000).
31. Borghs, G., Bhattacharyya, K., Deneffe, K., Van Mieghem, P. & Mertens, R. Band-gap narrowing in highly doped n- and p-type GaAs studied by photoluminescence spectroscopy. *Journal of Applied Physics* **66**, 4381-4386 (1989).
32. Miller, O. D., Yablonovitch, E. & Kurtz, S. R. Strong Internal and External Luminescence as Solar Cells Approach the Shockley&Queisser Limit. *Photovoltaics, IEEE Journal of* **2**, 303-311, doi:10.1109/jphotov.2012.2198434 (2012).

© 2013 **Macmillan Publishers Limited. All rights reserved.**